International Journal of Climatology

SPECIAL ISSUE Advances in Machine Learning for Weather and Climate: Modelling, Forecasting, and Applications

International Journal of Climatology RMetS

RESEARCH ARTICLE OPEN ACCESS

Improving Daily Rainfall Downscaling Over Taiwan's Complex Terrain With Surface-Wind-Informed Deep Learning Model

Yi-Chi Wang[1,2] | Chia-Hao Chiang[2] | Chiung-Jui Su[2] | Ko-Chih Wang[3] | Wan-Ling Tseng[4] | Hsin-Chien Liang[2]

[1]Swedish Meteorological and Hydrological Institute, Norrköping, Sweden | [2]Research Center for Environmental Changes, Academia Sinica, Taipei, Taiwan | [3]Department of Computer Science, National Taiwan Normal University, Taipei, Taiwan | [4]Institute of Sustainable Development and Climate Policy, National Tsing Hua University, Hsinchu, Taiwan

Correspondence: Ko-Chih Wang (kcwang@ntnu.edu.tw)

Received: 12 April 2026 | **Revised:** 11 September 2026 | **Accepted:** 16 September 2026

Keywords: bias correction | climate downscaling | deep neural network | orographic rainfall | Taiwan

ABSTRACT

This study evaluates whether an encoder-decoder deep neural network with multi-head attention can bias-correct and downscale ERA5 daily rainfall to Taiwan's 5-km TCCIP gridded observations. The Encoder–Decoder with Attention (EDA) model ingests ERA5 rainfall, 10-m winds, coarsened TCCIP rainfall, and 5-km topography, is trained with consecutive-year splits and a weighted MSE loss, and is benchmarked against bias correction spatial disaggregation (BCSD) and a rainfall-only variant. Across Taiwan's five seasonal rainfall regimes, EDA improves the placement of orographic rainfall, reduces the low-intensity wet bias in ERA5, and better reproduces RX1day (annual maximum 1-day precipitation), RX10mm (number of days with daily precipitation ≥ 10 mm), CDD (maximum number of consecutive dry days), and interannual variability than BCSD. The largest gains occur in seasons dominated by monsoon and typhoon forcing, indicating that auxiliary wind information helps the network learn the statistical relationships that better reproduce rainfall patterns associated with synoptic flow interacting with complex topography. The results show that attention-based statistical downscaling can improve the reproduction of high-resolution gridded rainfall fields for regions with steep terrain.

1 | Introduction

Localized rainfall information is essential for Taiwan because daily precipitation varies sharply across short distances under the combined influence of steep terrain, seasonal monsoon flow, and synoptic systems, such as typhoons and Meiyu. These localized rainfall patterns are central to flood risk, water-resource management, and climate-impact assessment, yet coarse-resolution reanalysis and climate-model products cannot resolve the terrain-controlled contrasts that shape rainfall over the island. Downscaling is therefore needed to translate large-scale climate information into local rainfall statistics relevant to Taiwan.

Climate downscaling is commonly approached through dynamical and statistical methods (Maraun et al. 2010). Dynamical downscaling uses regional climate models to simulate local climate variability and can better capture heavy rainfall when model resolution is sufficiently high (Westra et al. 2014), but it is computationally expensive and difficult to apply to large ensembles. Statistical downscaling instead constructs empirical relationships between large-scale predictors and local-scale predictands (Maraun and Widmann 2018). Within this family, model output statistics and quantile-mapping methods are attractive for bias correction, but their performance varies across applications and they often struggle with rainfall extremes, spatial displacement,

This is an open access article under the terms of the Creative Commons Attribution License, which permits use, distribution and reproduction in any medium, provided the original work is properly cited.

© 2026 The Author(s). *International Journal of Climatology* published by John Wiley & Sons Ltd on behalf of Royal Meteorological Society.

and terrain-controlled precipitation structure (Maraun and Widmann 2018; Soares et al. 2019; Vogel et al. 2023; Maraun et al. 2017).

Recent advances in deep learning have expanded the toolkit of statistical downscaling by enabling nonlinear mappings between coarse atmospheric fields and local climate responses (LeCun et al. 2015; Reichstein et al. 2019). Motivated in part by super-resolution methods from computer vision (Dong et al. 2014), deep-learning models such as DeepSD and related variants have been applied to climate downscaling over the United States and India (Vandal et al. 2017; Kumar et al. 2021; Wang et al. 2021; Sha et al. 2020). Encoder-decoder and related architectures have further shown that auxiliary predictors can improve rainfall downscaling and bias correction, whether using rainfall alone, surface variables, or broader atmospheric fields (Liu et al. 2020; Rocha Rodrigues et al. 2018; Saha and Ravela 2022; Sun and Tang 2020; Oyama et al. 2023; Wang et al. 2023; Harris et al. 2022; Price and Rasp 2022; Baño-Medina et al. 2020, 2021; Adewoyin et al. 2021; Sun and Lan 2021). However, rainfall over complex terrain remains difficult because the model must represent additional rainfall features that result from interactions between smaller-scale circulations and topography rather than only refine a precipitation image.

This challenge is particularly pronounced in Taiwan, where major mountain ranges exceeding 4000 m are confined within a narrow island (Figure 1a), producing strong spatial contrasts in rainfall. The island's precipitation is governed by distinct seasonal circulation regimes, including the spring transition, the Meiyu frontal system, the summer southwesterly monsoon, typhoon activity, and the winter northeast monsoon. Figure 1b illustrates the climatological annual rainfall cycle together with the time periods defining the five rainfall seasons adopted throughout this study. The resulting seasonal rainfall climatology exhibits substantial spatial variability, reflecting the interaction between large-scale atmospheric forcing and Taiwan's complex topography (Figure 1c; Chen and Chen 2003; Henny et al. 2021). Taiwan therefore provides a physically demanding testbed for evaluating whether a downscaling model can capture both localized rainfall

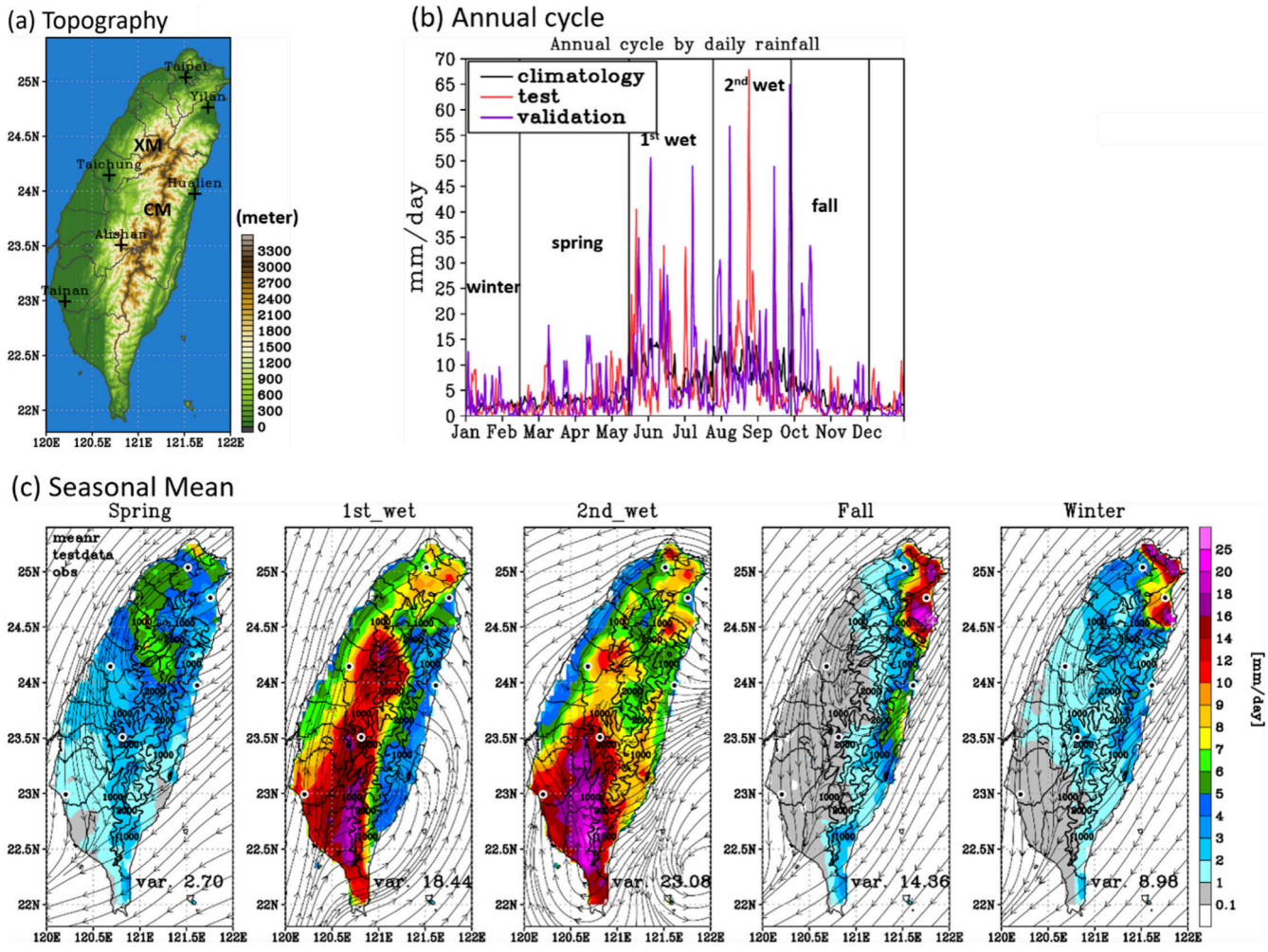

FIGURE 1 | (a) Taiwan's topography and six observational stations, highlighting Xue Mountain (XM) and Central Mountain (CM). (b) The annual rainfall cycle using the gridded observational TCCIP dataset, comparing the climatological mean (black), test period (red), and validation period (purple). (c) Mean rainfall (mm/day) from TCCIP and mean near-surface streamline of winds from ERA5 across Taiwan's five seasons during the test period. Elevation contours at 1000 and 2000 m are represented by thick black lines, and the boundaries of each county in Taiwan are depicted with fine black lines. [Colour figure can be viewed at wileyonlinelibrary.com]

10970088, 2026, 0, Downloaded from https://rmets.onlinelibrary.wiley.com/doi/10.1002/joc.70607. By Statens Beredning, Wiley Online Library on [20/10/2026]. See the Terms and Conditions (https://onlinelibrary.wiley.com/terms-and-conditions) on Wiley Online Library for rules of use; OA articles are governed by the applicable Creative Commons License

TABLE 1 | Data sources, spatial resolutions, variables, and their roles in the training and inference configurations of the EDA model.

Dataset	Original resolution/ domain	Period	Variable	Role in training	Role in validation/test
ERA5 reanalysis	25 km/global	1960–2020	Daily rainfall	Primary rainfall input	Primary input and also supplied to the auxiliary rainfall input channel
ERA5 reanalysis	25 km/global	1960–2020	10-m *u* and *v* winds	Encoder input	Encoder input
TCCIP daily rainfall	5 km/Taiwan land	1960–2020	Daily rainfall	High-resolution prediction target	Reference only for validation and evaluation
TCCIP daily rainfall, spatially aggregated	Aggregated coarse resolution to 25 km	Training period only	Coarse-resolution rainfall	Auxiliary encoder input	Not used
Taiwan topography	Taiwan land; interpolated to the 5-km grid	Static	Altitude	Decoder input	Decoder input

structures and the coupling between large-scale circulation and topography.

Chiang et al. (2024) demonstrated that an encoder–decoder model can improve rainfall prediction over Taiwan compared with traditional bias correction methods. However, several limitations remain for climate-oriented downscaling applications. Their approach relies on random data partitioning, which does not reflect temporal generalization to future climates, and employs a standard mean squared error loss that tends to underrepresent extreme rainfall, and the model does not explicitly incorporate key physical drivers, such as circulation and topographic effects. To address these limitations, the present study expands their framework in several ways. We adopt a sequential training, validation, and test strategy, introduce attention-based mechanisms and a weighted loss function to better capture intense rainfall, while explicitly including 10-m surface winds, coarsened high-resolution rainfall, and topography as auxiliary inputs. We refer to this model as the Encoder–Decoder with Multi-head Attention for auxiliary channels (EDA). An ablation experiment (EDA_PR) is further conducted to isolate the contribution of surface winds and evaluate performance across rainfall regimes, statistics, and extremes.

To address these goals, we use rainfall and 10-m winds from the fifth-generation European Centre for Medium-Range Weather Forecasts reanalysis dataset (ERA5; Hersbach et al. 2020) as coarse-resolution predictors, together with gridded 5-km rainfall observations over Taiwan as the target field, and high-resolution topography as a static auxiliary input. The proposed EDA model is evaluated against the bias correction spatial disaggregation (BCSD) benchmark, with emphasis on seasonal mean rainfall, extreme indices, station-scale statistics, interannual variability, and selected extreme event cases. Beyond model comparison, we provide a multi-perspective evaluation matrix to assess DL-based downscaling in a climate context, aiming to support future model development and establish a basis for systematic benchmarking. The remainder of the paper describes the data and model design, presents the comparative evaluation, and discusses the physical interpretation and limitations of the downscaling results.

2 | Data and Methods

2.1 | Data

In this study, we use daily rainfall data from two sources: the ERA5 (Hersbach et al. 2020) and high-resolution gridded observations from the Taiwan Climate Change Projection Information and Adaptation Knowledge Platform (TCCIP; Lin et al. 2022). ERA5 provides coarse-resolution input at 25 km, while TCCIP offers 5 km observations over Taiwan, serving as the reference for model evaluation. The time range and resolution for all the data are listed in Table 1.

ERA5 combines global numerical weather prediction with extensive observations through data assimilation and provides a homogeneous dataset for large-scale atmospheric states; however, its coarse resolution and parameterization-related biases can limit performance in regions with localized rainfall associated with strong circulation–topography interactions (e.g., Rivoire et al. 2021). We therefore use both ERA5-derived daily accumulated rainfall from hourly data along with 10-m winds as input as predictors.

The selection of 10-m surface winds as the sole auxiliary atmospheric predictor is guided by several physical and methodological considerations. First, near-surface winds represent the most direct dynamic variable interacting with high-resolution topography to govern orographic rainfall patterns, such as windward enhancement and leeward drying. Second, this approach follows the principle of parsimony, aiming to

10970088, 2026, 0, Downloaded from https://rmets.onlinelibrary.wiley.com/doi/10.1002/joc.70607. By Statens Beredning, Wiley Online Library on [20/10/2026]. See the Terms and Conditions (https://onlinelibrary.wiley.com/terms-and-conditions) on Wiley Online Library for rules of use; OA articles are governed by the applicable Creative Commons License

build upon the simplest possible univariate framework. By limiting auxiliary information to a minimal set of high-impact variables, we reduce the risk of model overfitting while ensuring the framework's portability across diverse Global Climate Models (GCMs) that may have limited variable availability. Finally, while thermodynamic factors (e.g., humidity and precipitable water) and large-scale steering (e.g., 850-hPa winds) are essential for rainfall formation, these variables are partially implicitly represented within the coarse-resolution ERA5 rainfall field itself. Consequently, 10-m winds serve as the necessary dynamic constraint to recover fine-scale spatial structures from the reanalysis input.

The TCCIP gridded rainfall dataset is constructed from observations at 2203 stations across Taiwan. Station data are interpolated onto a 5 km grid using objective analysis with Gaussian latent variables (Weng and Yang 2018). The dataset spans 1960–2020 and has been widely used in climate studies, including analyses of extreme rainfall trends (Tung et al. 2022; Henny et al. 2021, 2023), providing a robust ground truth for county-scale assessments. While the TCCIP dataset provides the high-resolution reference necessary for this study, it is essential to acknowledge that it is a gridded analysis product derived from stations via objective analysis, rather than a direct in situ observation (Lin et al. 2022; Weng and Yang 2018). Consequently, the dataset contains inherent interpolation uncertainties, which are most pronounced over Taiwan's complex mountainous terrain where station density is relatively sparse (Tung et al. 2022; Weng and Yang 2018). Previous evaluations of the TCCIP product indicate that the root-mean-square error (RMSE) between grid points and station observations is highest during the summer (JJA) and autumn (SON) rainy seasons (Weng and Yang 2018). Specifically, errors on the southwest windward slopes can range from 30 to 50 mm/day on average and may reach up to 55 mm/day in remote mountainous areas during the typhoon season (Tung et al. 2022; Weng and Yang 2018). Furthermore, the spatial homogenization involved in creating a 5-km grid can introduce effects, which tends to overestimate the frequency of light rainfall events (< 1 mm/day) while smoothing out localized extreme peaks (Weng and Yang 2018) compared with station pointwise observations.

We focus on Taiwan (22°–25° N, 120°–122° E) and use topographic data from the Terra Advanced Spaceborne Thermal Emission and Reflection Radiometer (ASTER) Global Digital Elevation Model (GDEM; NASA/METI/Japan Space Systems and U.S./Japan ASTER Science Team 2019). The original 20 m resolution data are regridded to 5 km with mean operation to match the 5-km gridded analysis of TCCIP rainfall dataset. Topography is treated as a static auxiliary field, enabling the model to represent key orographic effects, including windward enhancement, leeward drying, and sharp elevation gradients that govern rainfall distribution across the island.

2.2 | Training and Validating Procedure

Statistical downscaling fundamentally aims to establish functional relationships between the expected value of local-scale predictands Y and the large-scale predictors X, as outlined by Maraun et al. (2010). This relationship can be expressed as follows:

$$E(Y|X) = f(X, Q) \tag{1}$$

where f represents the nonlinear mapping function of downscaling, and Q represents the adjustable parameters optimized during the training process. In our study, Y is the high-resolution (5-km) TCCIP rainfall field. During training, X consists of four predictor fields: ERA5 rainfall, an auxiliary 25-km spatially aggregated rainfall field, and the ERA5 10-m zonal and meridional wind components The spatially aggregated rainfall field serves as an auxiliary predictor and is derived from the TCCIP rainfall during training, whereas it is replaced by ERA5 rainfall during inference, allowing the trained model to operate without requiring observational rainfall.

We divide the record into training (1960–2014), validation (2015–2017), and test (2018–2020) periods. This sequential split avoids information leakage and better reflects the way downscaling models are used for future prediction. The full record contains 22,281 daily precipitation samples, with approximately 80% for training, 10% for validation, and 10% for testing. Our choice of temporal division is designed to mimic typical practices in climate science, aiming for forecasts of future climate changes in a sequential manner rather than employing the random splitting commonly used in data science fields.

Before training, rainfall values are transformed with log1p to reduce skewness and enforce non-negative predictions, using fixed parameters derived exclusively from the training period. The primary ERA5 rainfall input and the 5-km TCCIP target were first transformed using $z = \log(1 + p)$. They were then independently normalized using

$$z^* = \frac{z}{z_{\max,\text{train}}}$$

where $z_{\max,\text{train}} = \log\left(1 + p_{\max,\text{train}}\right)$ and the minimum was fixed at zero because daily precipitation is non-negative. Separate maximum values were used for the ERA5 rainfall input, spatially aggregated TCCIP input, and 5-km TCCIP target. All training-derived normalization parameters were applied unchanged to the validation and test periods. Model rainfall predictions p_{pred} were converted to physical units using

$$p_{\text{pred}} = \exp\left(y * z_{\max,\text{train}}\right) - 1$$

where y is the normalized rainfall predicted by the model. However, because the inverse log1p transformation is nonlinear, differences in log space correspond to larger absolute differences at higher rainfall intensities after back-transformation. All features are then scaled to standardized range for consistency: log-transformed precipitation data is normalized to a [0, 1] range, while the 10-m wind components are scaled to a [−1, 1] range. Collectively, these preprocessing steps stabilize optimization and reduce sensitivity to extreme values. Normalization statistics are computed strictly from the training set and applied consistently to the validation and test sets to prevent data leakage.

10970088, 2026, 0, Downloaded from https://rmets.onlinelibrary.wiley.com/doi/10.1002/joc.70607. By Statens Beredning, Wiley Online Library on [20/10/2026]. See the Terms and Conditions (https://onlinelibrary.wiley.com/terms-and-conditions) on Wiley Online Library for rules of use; OA articles are governed by the applicable Creative Commons License

2.3 | Model Structure: Encoder-Decoder With Multi-Head Attention Layers for Auxiliary Channels

The DL-based model, Encoder-Decoder with multi-head Attention layers for auxiliary channels (EDA), builds upon the framework of Chiang et al. (2024) and consists of two main components: an encoder and a decoder. The design of the model is guided by the need to effectively represent spatial dependencies and physical relationships in climate variables, particularly for regions with complex terrain such as Taiwan. In the encoder, we adopt a multi-head attention mechanism inspired by the Transformer architecture (Vaswani et al. 2017) to complement conventional feature extraction approaches. This configuration allows the model to capture spatial dependencies across the domain, enabling each grid point to account for information from both local and remote regions. Such capability is particularly relevant for climate applications, where precipitation patterns are influenced by interactions across multiple spatial scales.

The datasets and their stage-specific roles are summarized in Table 1, while Figure 2 illustrates how the inputs are processed within the EDA architecture. The encoder is responsible for extracting representative features from the input climate variables and identifying spatial relationships among grid points. During training, the four predictor fields described in Section 2.2, including ERA5 rainfall, the auxiliary spatially aggregated rainfall field, and the ERA5 10-m zonal and meridional wind components, are concatenated along the channel dimension before being transformed into high-dimensional feature representations by the encoder. The attention mechanism then facilitates the identification of coherent spatial patterns and dependencies, allowing the model to highlight regions that contribute most strongly to rainfall variability. In this context, the attention layers can be interpreted as a data-driven way to capture large-scale circulation influences and their interaction with regional features. The decoder component retains a convolutional neural network structure, which is well suited for reconstructing spatially coherent high-resolution fields. The encoded features are reshaped back into two-dimensional grids and combined with topographic information before being passed through the decoder. This design enables the model to explicitly account for terrain effects, such as orographic enhancement of precipitation. In this study, we adopt super-resolution CNN-based approaches (Dong et al. 2014; Shi et al. 2016) to learn the nonlinear mapping from coarse-resolution inputs to fine-scale rainfall. Downscaling is achieved through a one-step upscaling process using pixel-shuffling techniques (Shi et al. 2016), which efficiently increase spatial resolution while preserving learned feature relationships. By integrating encoded large-scale information with local topographic features, the model is able to better reproduce rainfall patterns associated with the interactions between atmospheric circulation and terrain that govern rainfall distribution.

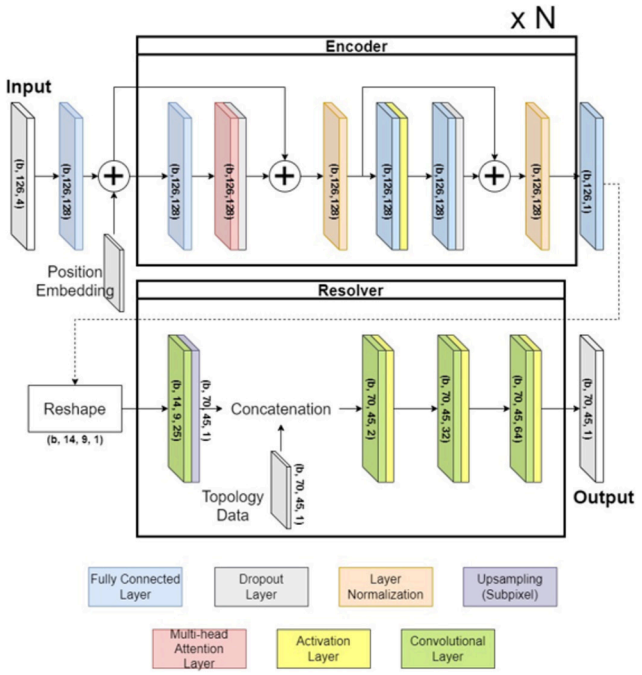

FIGURE 2 | Model architecture of the Encoder–Decoder with Multi-Head Attention for Auxiliary Channels (EDA) Model. '*N*' represents an adjustable parameter that dictates the repetition frequency of model components. Data dimensions at each layer are annotated, with 'b' indicating the batch size utilized. [Colour figure can be viewed at wileyonlinelibrary.com]

During validation, testing, and inference, spatially aggregated TCCIP rainfall is not used because it is derived from the observational target dataset and cannot be assumed to be available for new prediction periods. This auxiliary channel is therefore replaced by ERA5 rainfall, such that ERA5 rainfall is supplied to both rainfall channels, while the ERA5 10-m zonal and meridional wind inputs remain unchanged. The spatially aggregated TCCIP channel is used during training to provide an observation-constrained coarse-resolution rainfall representation, enabling the encoder to first learn a coarse-resolution bias-correction mapping before the decoder learns the super-resolution mapping to 5-km rainfall. Maintaining a separate auxiliary rainfall channel also provides flexibility to incorporate a higher-quality rainfall analysis in future applications without modifying the model architecture. In the present test configuration, using ERA5 in both rainfall channels represents the least observation-constrained configuration considered and therefore provides a conservative evaluation based exclusively on ERA5 predictors. Nevertheless, replacing the spatially aggregated TCCIP rainfall used during training with ERA5 rainfall introduces a difference between the training and inference input distributions, which is acknowledged as a limitation of the current implementation. To prevent information leakage, TCCIP rainfall from the validation and test periods is never supplied as a model input and is used only as the reference for model evaluation. We implemented the model in TensorFlow with a batch size of 64 and a maximum of 1000 epochs. Training uses Adam with a learning rate of 1e-4 and early stopping after 60 epochs without improvement. The model was trained on an NVIDIA Tesla V100 GPU and completed in a little over 10 h. Our model employs a weighted mean square error (WMSE) as the loss function as follows:

$$\mathrm{WMSE} = \frac{1}{HW}\sum_{i=1}^{H}\sum_{j=1}^{W}\left[\gamma\widehat{Y_{ij}}\left(\widehat{Y_{ij}}-Y_{ij}\right)^2+(1-\gamma)\left(\widehat{Y_{ij}}-Y_{ij}\right)^2\right], \gamma\in[0,1] \quad (2)$$

10970088, 2026, 0, Downloaded from https://rmets.onlinelibrary.wiley.com/doi/10.1002/joc.70607. By Statens Beredning, Wiley Online Library on [20/10/2026]. See the Terms and Conditions (https://onlinelibrary.wiley.com/terms-and-conditions) on Wiley Online Library for rules of use; OA articles are governed by the applicable Creative Commons License

where H and W are the height and width (i.e., the numbers of grid cells in the latitude and longitude directions) of the output rainfall field, Y_{ij} is the prediction and $\widehat{Y_{ij}}$ is the corresponding ground truth at grid cell (i, j). The weighting factor $\gamma \in [0, 1]$ controls the relative importance assigned to high-rainfall regions during training, with larger values giving greater emphasis to heavy rainfall while smaller values approach the standard mean squared error. This approach sets higher penalties on errors in regions characterized by high rainfall and it addresses the need for better prediction of extreme weather events. The distribution of rainfall is strongly right-skewed, which means that weak-rain and dry days dominate the samples. Therefore, an unweighted MSE is dominated by these cases, and the gradient contribution of rare heavy-rainfall events during training is small. The weighting reallocates the sample weight toward the high-error samples, which are usually the samples at the tail of the distribution. The model also applies $\log 1p$ normalization to the target rainfall fields. This logarithmic transform is a common practice that stabilizes the optimization by compressing the dynamic range. However, it may also suppress the gradients associated with extremes, and the weighted loss can also balance this effect.

The model is trained using a two-stage supervised procedure (see Algorithm S1). In the first stage, the encoder is trained using the normalized low-resolution rainfall and wind predictors of ERA5 to reproduce TCCIP rainfall bilinearly downsampled to the encoder output resolution. In the second stage, the trained encoder parameters are frozen, and the decoder is optimized to reconstruct the full-resolution TCCIP rainfall field from the encoded features together with the high-resolution topographic information. The WMSE loss function is used in both stages, and early stopping is applied based on the corresponding validation loss. This sequential procedure first constrains the encoder to extract rainfall-relevant large-scale features and then trains the decoder to perform spatial downscaling and bias correction.

2.4 | Baseline Downscaling Methods: Bias Correction Spatial Disaggregation Method

For benchmarking within the univariate downscaling framework in our study, we have adopted the BCSD method as our comparative baseline. Developed by Wood et al. (2002), BCSD merges spatial and temporal disaggregation for downscaling with a quantile mapping (QM)-based technique for bias correction, designed to align the modelled data distribution with the observed distribution over corresponding periods effectively. This method is notable for its capability to maintain the mean percentile of data distribution efficiently, its computational effectiveness, and its independence from requiring prior specific information, making it widely used in regional studies (Bürger et al. 2013; Cannon et al. 2015; Maraun et al. 2010), including that focused on Taiwan by TCCIP (Lin et al. 2023). However, BCSD, as a representative QM downscaling method, shares common challenges associated with QM-type methods, including potential shifts on the tails of the distribution, the incapability to correct misrepresenting location bias in coarse-resolution datasets (Maraun and Widmann 2018, 2015; Maraun et al. 2017), as well as the challenge in preserving long-term climate trends within the data (Cannon et al. 2015).

In our current implementation of BCSD, we have omitted the original design of the temporal disaggregation step for converting monthly-resolved data into a daily time scale and adopted a step with daily rainfall data in line with the methodologies of recent studies (Thrasher et al. 2012; Vandal et al. 2019). For other details, we adhere closely to the methodological framework for statistical downscaling in Taiwan with CMIP6 models, as outlined by Lin et al. (2023), including the three steps below:

1. First, the ERA5 rainfall data is bilinearly interpolated onto the TCCIP data grid, transitioning from 25 to 5 km grids to align with the TCCIP dataset's fine-scale resolution.
2. Subsequently, employing a 31-day time window centred around the target day for each grid point, we construct the cumulative distribution function (CDF) in a manner that effectively captures the climatological distribution, using 61 years of TCCIP gridded rainfall data. A bin width of 15%, determined through empirical testing, is applied in constructing the CDF for each grid point.
3. The final step is to adjust the interpolated coarse-resolution rainfall data to the observational rainfall's corresponding CDF quantiles using the QM method.

2.5 | Evaluation Metrics

Here, we have listed model metrics that we used in understanding the performance of downscaling methods. First, to evaluate the ability of each method to reproduce the observed spatial distribution of rainfall, all the metrics are computed first with respect to the five rainfall seasons based on all daily rainfall fields within each season during the corresponding validation or test period. The resulting fields from ERA5, BCSD, and EDA are then compared with the TCCIP reference dataset.

To assess whether the proposed deep learning methods provide statistically significant improvements over the baseline BCSD approach, statistical significance tests were conducted for the evaluation metrics reported. For each evaluation period, season, and climate index, the performance of EDA and EDA_PR was compared against BCSD using paired statistical resampling based on the corresponding evaluation samples. A performance improvement was considered statistically significant when the null hypothesis of no difference between the methods was rejected at the 95% confidence level ($p < 0.05$). Statistically significant improvements over BCSD are denoted by a dagger superscript (†) in the corresponding tables.

2.5.1 | Correlation and Root-Mean-Square Error

The similarity of the spatial rainfall patterns is quantified using the Pearson correlation coefficient (CORR) and the RMSE, both computed over all land grid cells of Taiwan.

Let O_i and P_i denote the observed (TCCIP) and predicted rainfall at grid cell i, respectively, and N be the total number of land grid cells. CORR is calculated as

10970088, 2026, 0, Downloaded from https://rmets.onlinelibrary.wiley.com/doi/10.1002/joc.70607. By Statens Beredning, Wiley Online Library on [20/10/2026]. See the Terms and Conditions (https://onlinelibrary.wiley.com/terms-and-conditions) on Wiley Online Library for rules of use; OA articles are governed by the applicable Creative Commons License

$$\mathrm{CORR}=\frac{\sum_{i=1}^{N}\left(P_i-\overline{P}\right)\left(O_i-\overline{O}\right)}{\sqrt{\sum_{i=1}^{N}\left(P_i-\overline{P}\right)^2}\sqrt{\sum_{i=1}^{N}\left(O_i-\overline{O}\right)^2}} \tag{3}$$

where $\overline{P}$ and $\overline{O}$ denote the spatial mean rainfall over Taiwan.

RMSE is calculated as follows:

$$\mathrm{RMSE}=\sqrt{\frac{1}{N}\sum_{i=1}^{N}\left(P_i-O_i\right)^2} \tag{4}$$

CORR measures the similarity of the spatial rainfall pattern independent of the absolute rainfall magnitude, whereas RMSE quantifies the magnitude of spatial errors. Both are computed directly from the climatological rainfall fields without any additional normalization or bias correction. These two complementary metrics are widely used in climate downscaling studies to assess both the reproduction of spatial rainfall structures and the accuracy of rainfall intensity.

2.5.2 | ETCCDI Indices

To quantify the performance of rainfall extremes of downscaling methods, we have also used the extreme indices developed by the joint Expert Team on Climate Change Detection and Indices (ETCCDI) of the WMO Commission for Climatology and World Climate Research Programme Climate Variability and Predictability project (Karl et al. 1999; Frich et al. 2002; Zhang et al. 2011), which are widely used in many studies about extreme events, including in several IPCC reports (Sillmann et al. 2013). For the following definition of extreme indices, we have let RR_{ij} as the daily rainfall amount on day i in period j. Then the extreme indices defined as follows:

- RX1day (monthly maximum 1-day precipitation): $\mathrm{RX1day}_j=\max\left(\mathrm{RR}_{ij}\right)$ for a period j.
- CDD (maximum length of consecutive days with RR < 1 mm): The largest number of consecutive days when $\mathrm{RR}_{ij}<1$ mm of each day i in period j.
- RX10mm (annual count of days when $\mathrm{RR}_{ij}\geq 10$ mm): The number of rainy days when daily $\mathrm{RR}_{ij}>10$ mm in period j.

2.5.3 | Spatial Verification Metrics: Fraction Skill Score and Structure-Amplitude-Location Scores

To complement the grid-point-based correlation (CORR) and RMSE, we evaluated the spatial characteristics of daily rainfall using the Fractions Skill Score (FSS; Roberts and Lean 2008) and the Structure–Amplitude–Location (SAL; Wernli et al. 2008) metrics. Unlike pointwise verification, both methods are less sensitive to the double-penalty problem associated with small spatial displacement errors. FSS evaluates neighbourhood-scale agreement in rainfall occurrence, whereas SAL provides an object-based assessment of rainfall structure, intensity, and spatial displacement.

The FSS was used to evaluate the spatial agreement of daily rainfall exceedance patterns. For a rainfall threshold q, binary exceedance fields were first defined for the observations and model output,

$$I_{\mathrm{o}}(x)=\begin{cases}1, & R_{\mathrm{o}}(x)\geq q,\\ 0, & \text{otherwise},\end{cases}\quad I_{\mathrm{m}}(x)=\begin{cases}1, & R_{\mathrm{m}}(x)\geq q,\\ 0, & \text{otherwise}\end{cases} \tag{5}$$

Neighbourhood fractions were then computed within a moving window W_x,

$$f_{\mathrm{o}}(x)=\frac{1}{N_x}\sum_{y\in W_x}I_{\mathrm{o}}(y),f_{\mathrm{m}}(x)=\frac{1}{N_x}\sum_{y\in W_x}I_{\mathrm{m}}(y) \tag{6}$$

where N_x is the number of valid Taiwan land grid cells within the neighbourhood. Ocean and missing grid cells were excluded from the calculation. The daily FSS was computed as

$$\mathrm{FSS}=1-\frac{\sum_x\left[f_{\mathrm{o}}(x)-f_{\mathrm{m}}(x)\right]^2}{\sum_x f_{\mathrm{o}}(x)^2+\sum_x f_{\mathrm{m}}(x)^2} \tag{7}$$

with values ranging from 0 to 1, where larger values indicate better spatial agreement. Days with no rainfall exceedance in either observations or model output were excluded from the seasonal averages.

The SAL metric was used to evaluate object-based rainfall characteristics. Rainfall objects were identified from daily threshold exceedance fields using 8-neighbour connectivity and a minimum object-size criterion, applied consistently to both observations and model output over Taiwan land points. SAL consists of three complementary components. The amplitude component quantifies differences in domain-mean rainfall:

$$A=\frac{\overline{R}_{\mathrm{m}}-\overline{R}_{\mathrm{o}}}{0.5\left(\overline{R}_{\mathrm{m}}+\overline{R}_{\mathrm{o}}\right)} \tag{8}$$

where $\overline{R}_{\mathrm{o}}$ and $\overline{R}_{\mathrm{m}}$ denote the observed and modelled domain-mean rainfall, respectively.

The location component,

$$L=L_1+L_2 \tag{9}$$

combines the normalized distance between the rainfall-weighted centroids of the observed and modelled fields,

$$L_1=\frac{d\left(x_{\mathrm{m}},x_{\mathrm{o}}\right)}{d_{\max}} \tag{10}$$

with the difference in the spatial dispersion of rainfall objects around their respective centroids,

$$L_2=\frac{2\left|r_{\mathrm{m}}-r_{\mathrm{o}}\right|}{d_{\max}} \tag{11}$$

where $d_{\max}$ is the maximum land-to-land distance within the Taiwan domain.

The structure component compares the normalized volume characteristics of rainfall objects,

10970088, 2026, 0, Downloaded from https://rmets.onlinelibrary.wiley.com/doi/10.1002/joc.70607. By Statens Beredning, Wiley Online Library on [20/10/2026]. See the Terms and Conditions (https://onlinelibrary.wiley.com/terms-and-conditions) on Wiley Online Library for rules of use; OA articles are governed by the applicable Creative Commons License

$$S = \frac{V_m - V_o}{0.5\left(V_m + V_o\right)} \tag{12}$$

where V_o and V_m are the rainfall-weighted scaled volumes of the observed and modelled rainfall objects, respectively. Values of $S = 0$, $A = 0$, and $L = 0$ indicate perfect agreement between the modelled and observed rainfall fields.

3 | Results

3.1 | Seasonal Rainfall Mean for Five Seasons in Taiwan

Figure 1a shows the topography of Taiwan based on the ASTER GDEM dataset, highlighting the two mountain ranges, Xue Mountain and the Central Mountain Range. These north–south-oriented ranges exceed 2000 m and strongly interact with synoptic systems, shaping rainfall patterns across the island. Figure 1b presents the annual rainfall cycle derived from daily TCCIP data, including climatology, training, and validation periods. Five distinct seasons—spring, the first and second rainy seasons, autumn, and winter—are identified following previous studies (Chou et al. 2009; Table 2). Climatologically, rainfall increases from spring and peaks during the two summer rainy seasons, with mean values around 15 mm/day (black line in Figure 1b). However, this mean state masks pronounced variability, as short-duration extreme events substantially exceed the seasonal average. Daily rainfall frequently surpasses 30 mm/day during Meiyu frontal passages and can exceed 50 mm/day during typhoon events (red and purple lines in Figure 1b), indicating that a large fraction of seasonal totals is contributed by episodic, high-intensity rainfall. This strong contrast between mean conditions and extremes highlights the intermittency and event-driven nature of Taiwan's rainfall.

Figure 1c shows the observed spatial distribution of seasonal mean rainfall across Taiwan based on TCCIP data during the test period, while Figure 3 compares ERA5, BCSD, and EDA downscaling results against these patterns. The metrics of CORR and RMSE comparing BCSD and EDA against TCCIP are shown in Table 3. In spring, rainfall is concentrated over northwestern Taiwan, particularly along the southern slopes of Xue Mountain, consistent with frontal flow impinging on the terrain (Figure 1c). Compared with the TCCIP observations (Figure 1c), ERA5 misplaces this maximum over eastern Taiwan (Figure 3a), whereas both BCSD and EDA correct this displacement (Figure 3b,c). Compared with EDA, BCSD maintains a slight statistical advantage in this season, though both methods keep residual biases below 2 mm/day (Table 3). During the first rainy season, southwesterly monsoon flow transports moisture toward Taiwan, producing rainfall over the southwestern foothills of the CM range and central western Taiwan (Figure 1c). ERA5 overestimates rainfall along the eastern slopes and coastal regions, indicating a weaker alignment with the observed flow–topography structure. Relative to the TCCIP rainfall distribution, both BCSD and EDA redistribute rainfall toward the southwestern mountains, with EDA more closely capturing both the intensity (~15–20 mm/day) and spatial pattern (Figure 3b,c). In the second rainy season, typhoon-related cyclonic flow enhances moisture transport, leading to rainfall maxima over southwestern Taiwan and the eastern slopes of the CM (Figure 1d). Compared with TCCIP, ERA5 captures the southwestern maximum but overestimates rainfall in northern Taiwan (Figure 3a). Both BCSD and EDA improve the north–south contrast, with EDA better reproducing the observed asymmetry associated with storm-driven flow (Figure 3b,c). In autumn and winter, northeasterly monsoon flow produces windward enhancement over eastern and northeastern Taiwan (Figure 1c). While ERA5 overestimates rainfall along the eastern slopes (Figure 3a), both BCSD and EDA reduce this bias and better reproduce the observed windward distribution (Figure 3b,c). However, it is noteworthy that in the relatively stable regimes of autumn and winter, the BCSD achieves higher CORR and lower RMSE than the EDA model (Table 3). This suggests that while the attention-based EDA model excels at resolving the convective rainfall activities dominant in the summer wet seasons, the traditional BCSD method remains highly effective for the monsoonal rainfall by the northeasterly monsoon.

TABLE 2 | Definition of five raining seasons of Taiwan based on previous climatological studies (Chou et al. 2009).

Name	Time period
Spring	February 15–May 15
Summer first wet season	May 16–July 24
Summer second wet season	July 25–September 27
Autumn	September 28–December 1
Winter	December 2–February 14

3.2 | ETCCDI Extreme Indices

We analysed climate extreme indices as recommended by the ETCCDI using rainfall data from TCCIP, BCSD, and our EDA model. This analysis includes the maximum 1-day rainfall (RX1day; Figure 4), the number of days with intense rainfall exceeding 10 mm (RX10mm; Figure 5), and the longest stretch of consecutive dry days (CDD; Figure 6). In the meantime, the CORR and RMSE of each model and TCCIP observations are summarized in Table 4 for the ETCCDI indices.

Figure 4 illustrates the climatological distribution of maximum 1-day rainfall (RX1day) across five rainy seasons within the test period. During spring, the maximum of RX1day is predominantly observed over the northwest and on the southern edge of Xue Mountain (approximately 24°–24.5° N), with RX1day values reaching up to 60 mm/day. In the summer's wet seasons, RX1day values exceed 100 mm/day, with peaks up to 300 mm/day observed on the southwest slope of the Central Mountain. The magnitude of RX1day over the Xue Mountain diminishes gradually, with rainfall shifting toward the eastern slope of the Central Mountain, where it is influenced by typhoon-related rainfall from the tropical Pacific (Figure 4a). Both BCSD and EDA models exhibit comparable performances in spring, fall, and winter—seasons characterized by less extreme rainfall events. During the two wet seasons in summer, notably, both models tend to underestimate the extreme rainfall over the southwest slope of the Central

10970088, 2026, 0, Downloaded from https://rmets.onlinelibrary.wiley.com/doi/10.1002/joc.70607. By Statens Beredning, Wiley Online Library on [20/10/2026]. See the Terms and Conditions (https://onlinelibrary.wiley.com/terms-and-conditions) on Wiley Online Library for rules of use; OA articles are governed by the applicable Creative Commons License

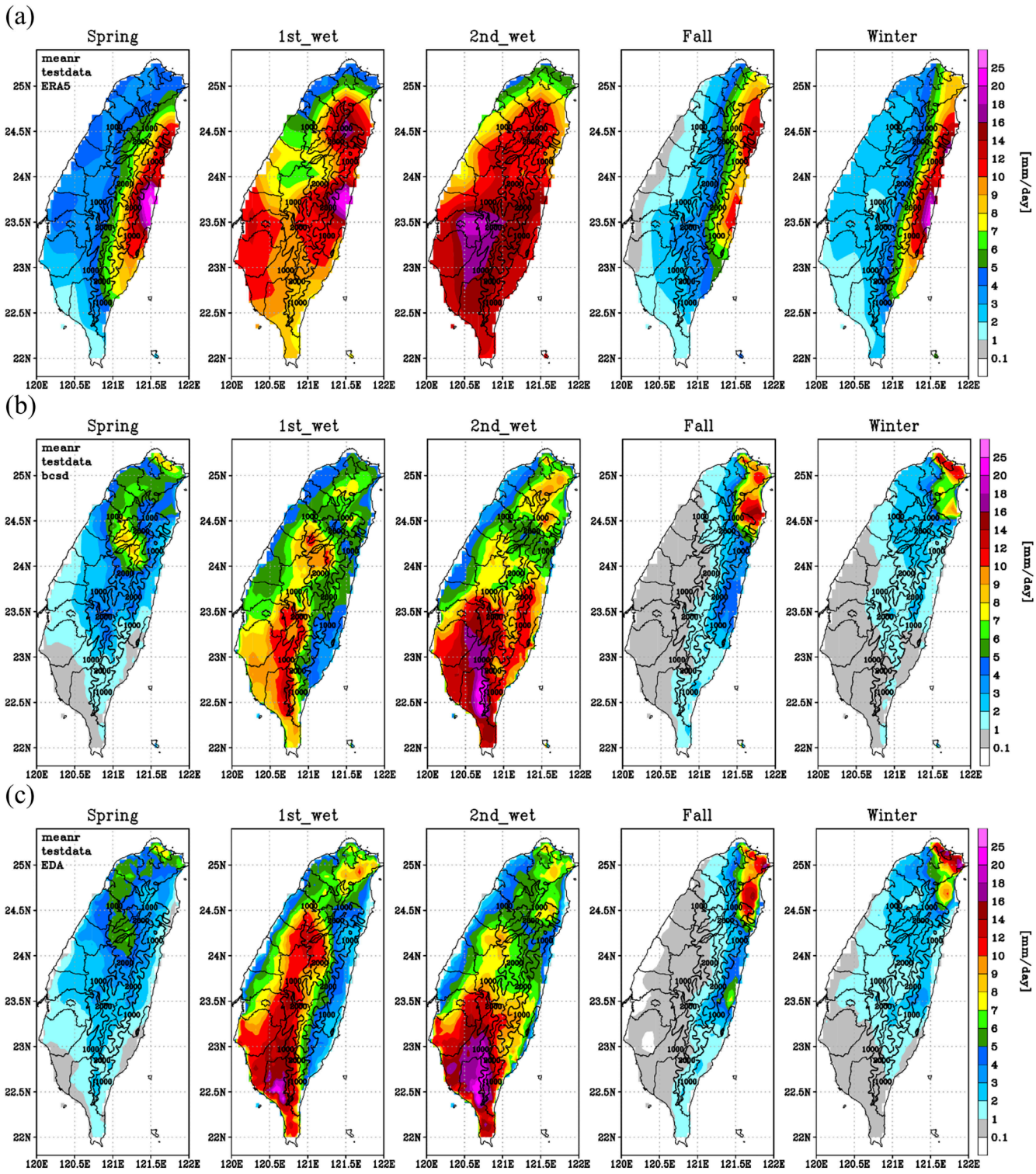

FIGURE 3 | Mean rainfall distribution of five rainy seasons defined in Table 2 with units of mm/day during test period (December 13, 2017 to December 31, 2020). (a) ERA5 reanalysis, (b) BCSD downscaled rainfall from ERA5, and (c) EDA downscaled rainfall from ERA5. Elevation contours at 1000 and 2000 m are represented by thick black lines, and the boundaries of each county in Taiwan are depicted with fine black lines. [Colour figure can be viewed at wileyonlinelibrary.com]

Mountain, with discrepancies of up to 50 mm/day in summer seasons (Figure 4b,c). Nonetheless, the EDA model displays a more random-like distribution of RX1day across southwest Taiwan, compared with the dry bias over southwestern Taiwan indicating a wider dry bias. Furthermore, EDA demonstrates a better capability to capture the rainfall over the eastern side of Taiwan in the first wet season and northern Taiwan in fall, compared to BCSD, suggesting a more accurate representation of rainfall extremes during the typhoon seasons (Figure 4b,c).

Figure 5 displays the spatial distribution of days experiencing rainfall exceeding 10 mm (RX10mm) as recorded by TCCIP and

10970088, 2026, 0, Downloaded from https://rmets.onlinelibrary.wiley.com/doi/10.1002/joc.70607. By Statens Beredning, Wiley Online Library on [20/10/2026]. See the Terms and Conditions (https://onlinelibrary.wiley.com/terms-and-conditions) on Wiley Online Library for rules of use; OA articles are governed by the applicable Creative Commons License

TABLE 3 | Performance metrics for mean rainfall for five rainy seasons in Taiwan.

CORR (RMSE)	Spring		First-wet		Second-wet		Fall		Winter	
	Test	Validation	Test	Validation	Test	Validation	Test	Validation	Test	Validation
MeanR										
BCSD	**0.93(0.74)**	**0.95(0.67)**	0.93(2.97)	0.92(2.24)	**0.94(1.75)**	**0.93(1.59)**	**0.97(1.50)**	**0.94(1.61)**	**0.95(1.42)**	**0.97(0.74)**
EDA	0.91(0.76)	0.94(0.77)	**0.94(1.79)**‡	**0.93(1.77)**‡	0.94(2.05)	0.89(2.12)	0.90(1.91)	0.91(1.78)	0.87(1.56)	0.89(0.93)
EDA_PR	0.87(1.25)	0.93(1.49)	0.91(4.78)	0.90(5.09)	0.91(4.30)	0.81(3.90)	0.94(2.73)	0.87(2.99)	0.91(2.24)	0.93(1.44)

Note: Bold values indicate the highest correlation coefficient among the downscaling methods. Underlined values indicate the lowest RMSE. A superscript (‡) indicates that the corresponding downscaling method performs significantly better than BCSD in CORR or RMSE at the 95% confidence level ($p < 0.05$).

contrasts the predictive discrepancies between BCSD and EDA during the test period. RX10mm is a critical measure for identifying days characterized by significant rainfall. Consistent with the overall mean rainfall distribution, the bulk of rainy days is concentrated during the first and second summer seasons, notably on the western slopes of the Central Mountain. Rainfall in the northeastern and eastern parts of Taiwan begins in fall and continues through winter (Figure 5a). Throughout the five seasons, BCSD tends to slightly underestimate the frequency of rainy days, a tendency mirrored by the EDA model. Notably, during the first wet season, BCSD shows a marked underestimation, missing rainy days by up to 10 days across the central mountains, particularly near the southern tip of Xue Mountain. This discrepancy arises as the ERA5 reanalysis inaccurately captures rainfall locations during the first wet season, challenging BCSD's ability to identify significant rainfall events despite its effectiveness in adjusting mean rainfall levels (Figure 5b). A similar pattern of underestimation by BCSD is observed for RX10mm hotspots in the northeastern part of Taiwan during fall and winter. However, the EDA model manages to mitigate BCSD's dry bias to a considerable extent, though it still portrays a drier Yilan region compared to observations (Figure 1a).

Figure 6 delineates the spatial distribution of CDD throughout the five rainy seasons. According to observations, CDD typically averages about 10 days during the rainy seasons of spring and summer, with a peak in fall across western Taiwan. This trend continues into winter when CDD can extend up to 20 days in southern Taiwan (Figure 6a). The bias exhibited by BCSD varies across different seasons (Figure 6b). In spring, BCSD appears to overpredict rainfall in southern Taiwan, which results in an underprediction of CDD. During the summer's wet seasons, BCSD consistently overestimates CDD throughout Taiwan. In fall, BCSD's predictions overestimate CDD in northeastern Taiwan and similarly overestimate CDD in western Taiwan. Winter, generally a dry season for western Taiwan, sees BCSD overestimating CDD in west-central Taiwan while underestimating it in the southwest. By contrast, the EDA model demonstrates a markedly lower bias in spring, summer, and winter, more closely aligning with the observed CDD patterns. Autumn remains the most challenging season for EDA in simulating CDD. Although EDA still exhibits lower overall bias than BCSD, it tends to underestimate dry-spell duration in parts of Taiwan. This reduced skill likely reflects the transitional nature of autumn, when intermittent tropical-cyclone activity and the developing northeast monsoon make the timing and persistence of dry spells more difficult to reproduce accurately. Comparisons using CORR and RMSE metrics further underscore the EDA model's superior performance across all seasons, with the notable exception of the second wet season during summer (Table 4). The challenge in accurately modelling this season may stem from the substantial contribution of typhoon-related rainfall, which, due to its somewhat stochastic nature compared with other seasons, complicates the precise prediction of rainfall distribution.

3.3 | Spatial Verification of Daily Rainfall: FSS and SAL Scores

To complement the grid-point verification, we further evaluated the spatial characteristics of daily rainfall using the FSS and the

10970088, 2026, 0, Downloaded from https://rmets.onlinelibrary.wiley.com/doi/10.1002/joc.70607. By Statens Beredning, Wiley Online Library on [20/10/2026]. See the Terms and Conditions (https://onlinelibrary.wiley.com/terms-and-conditions) on Wiley Online Library for rules of use; OA articles are governed by the applicable Creative Commons License

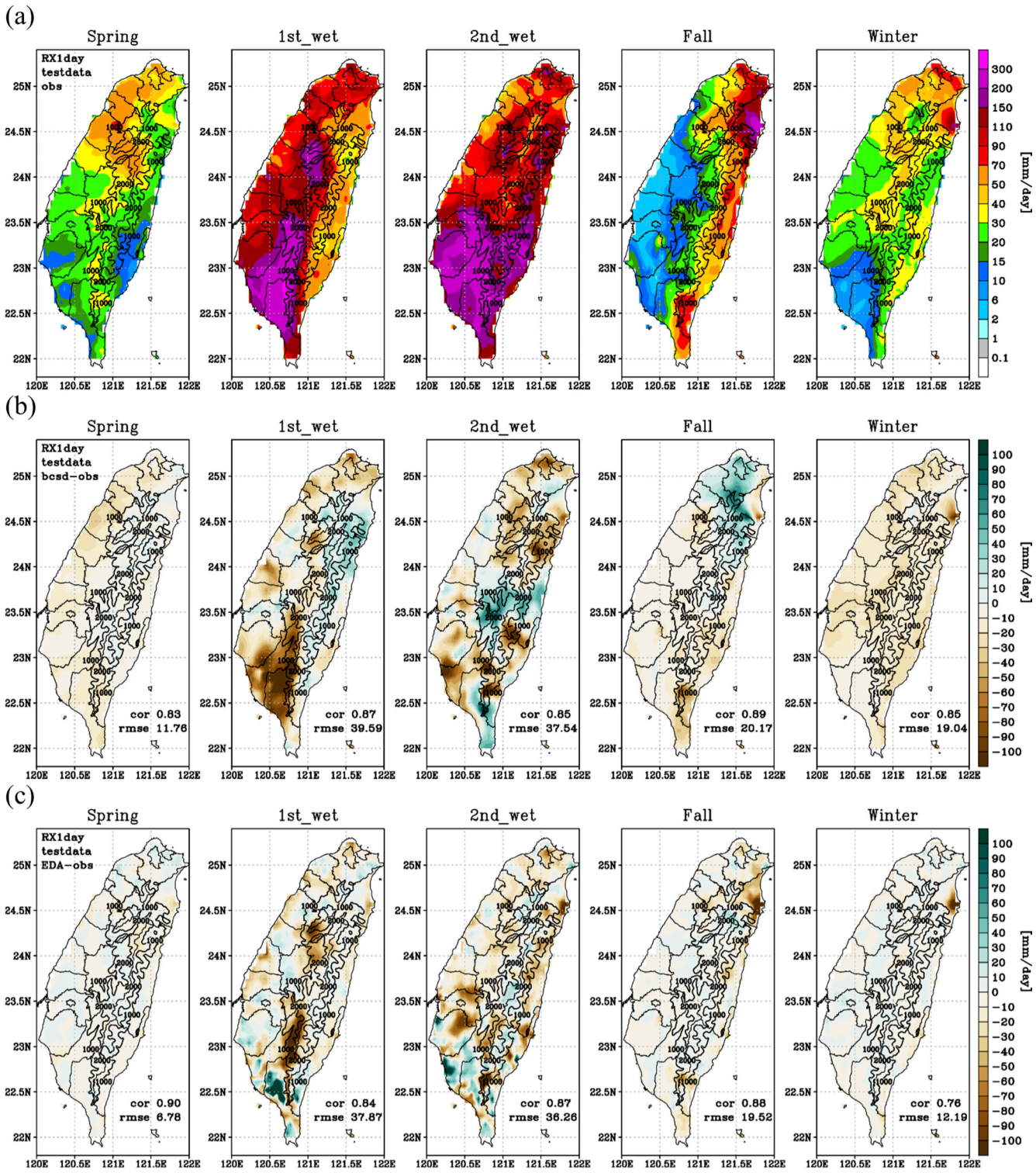

FIGURE 4 | (a) Spatial distribution of RX1day index from TCCIP observations and downscaled bias in (b) BCSD and (c) EDA model during test period (December 13, 2017 to December 31, 2020). Elevation contours at 1000 and 2000 m are represented by thick black lines, and the boundaries of each county in Taiwan are depicted with fine black lines. [Colour figure can be viewed at wileyonlinelibrary.com]

SAL metric. FSS assesses neighbourhood-scale agreement while reducing the double penalty associated with small spatial displacement errors, whereas SAL provides an object-based evaluation of rainfall structure, intensity, and spatial location.

Figure 7 presents the seasonal FSS for the 10 mm/day rainfall threshold. As expected, FSS increases with neighbourhood size for all methods because larger neighbourhoods allow greater tolerance for spatial displacement. Nevertheless, EDA consistently achieves the highest FSS across all seasons and neighbourhood scales, indicating that the incorporation of surface wind information substantially improves the spatial placement of moderate rainfall compared with BCSD and EDA_PR. The largest improvements are observed during the

10970088, 2026, 0, Downloaded from https://rmets.onlinelibrary.wiley.com/doi/10.1002/joc.70607. By Statens Beredning, Wiley Online Library on [20/10/2026]. See the Terms and Conditions (https://onlinelibrary.wiley.com/terms-and-conditions) on Wiley Online Library for rules of use; OA articles are governed by the applicable Creative Commons License

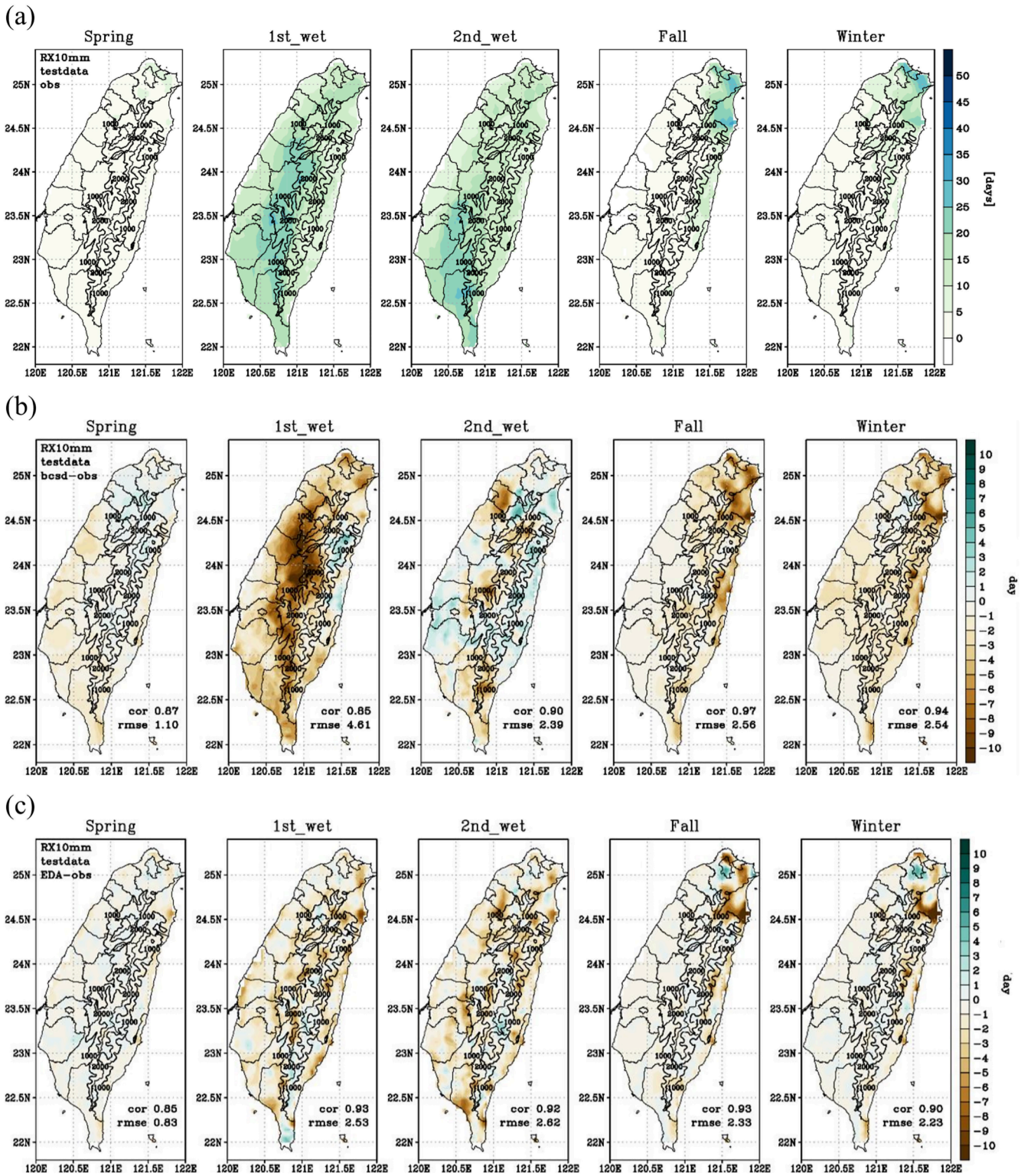

FIGURE 5 | (a) Spatial distribution of RX10mm index from TCCIP observations and downscaled bias in (b) BCSD and (c) EDA model during test period (December 13, 2017 to December 31, 2020). Elevation contours at 1000 and 2000 m are represented by thick black lines, and the boundaries of each county in Taiwan are depicted with fine black lines. [Colour figure can be viewed at wileyonlinelibrary.com]

two wet seasons, when rainfall is strongly controlled by the interaction between the southwesterly monsoon flow and Taiwan's complex terrain. Although FSS values are generally lower during spring and winter, reflecting the greater difficulty of reproducing rainfall occurrence during these transition seasons, EDA maintains a clear advantage throughout the year. FSS analysis with threshold 1 and 50 mm/day can be found in Figure S3.

The SAL analysis (Table 5) further demonstrates that these improvements extend beyond neighbourhood agreement. EDA consistently yields the smallest errors in all three SAL

10970088, 2026, 0, Downloaded from https://rmets.onlinelibrary.wiley.com/doi/10.1002/joc.70607. By Statens Beredning, Wiley Online Library on [20/10/2026]. See the Terms and Conditions (https://onlinelibrary.wiley.com/terms-and-conditions) on Wiley Online Library for rules of use; OA articles are governed by the applicable Creative Commons License

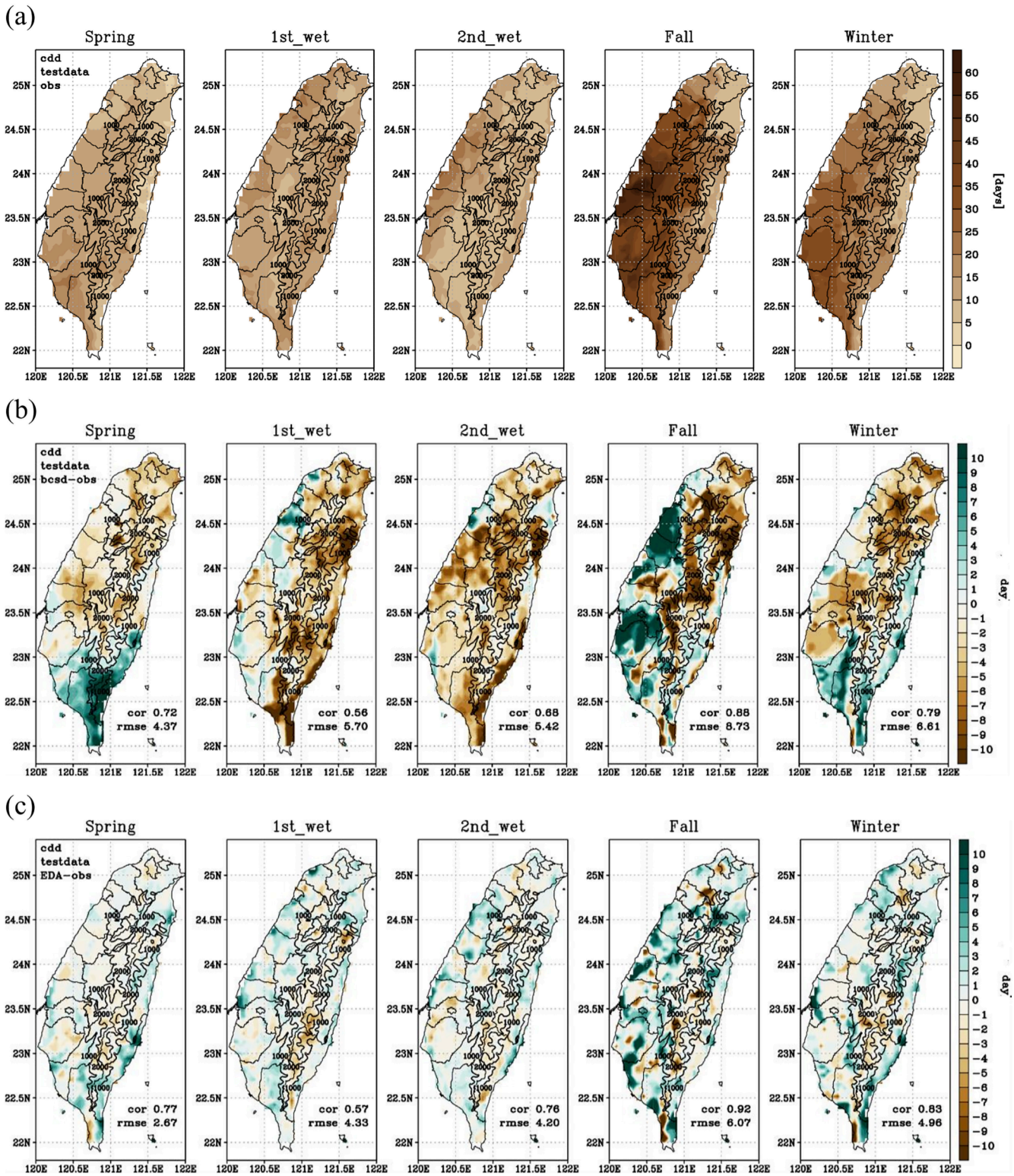

FIGURE 6 | Spatial distribution of CDD index from (a) TCCIP observations and downscaled bias with (b) BCSD and (c) EDA model during test period (December 13, 2017 to December 31, 2020). Elevation contours at 1000 and 2000 m are represented by thick black lines, and the boundaries of each county in Taiwan are depicted with fine black lines. [Colour figure can be viewed at wileyonlinelibrary.com]

components—structure (|S|), amplitude (|A|), and location (L)—across all five rainfall seasons. Moreover, every best-performing SAL metric is statistically significant at the 95% confidence level according to the paired bootstrap test, indicating that the improvements are robust rather than arising from sampling variability. The largest reductions are found for the amplitude and location components, suggesting that EDA more accurately reproduces both the overall rainfall intensity and the spatial positioning of rainfall systems. Compared with EDA_PR, which excludes surface wind information, the substantially lower SAL errors further demonstrate that incorporating surface winds improves not only the spatial overlap of

10970088, 2026, 0, Downloaded from https://rmets.onlinelibrary.wiley.com/doi/10.1002/joc.70607. By Statens Beredning, Wiley Online Library on [20/10/2026]. See the Terms and Conditions (https://onlinelibrary.wiley.com/terms-and-conditions) on Wiley Online Library for rules of use; OA articles are governed by the applicable Creative Commons License

TABLE 4 | Performance metrics for selected extreme indices for five rainy seasons in Taiwan.

	Spring		First-wet		Second-wet		Fall		Winter	
CORR (RMSE)	**Test**	**Validation**	**Test**	**Validation**	**Test**	**Validation**	**Test**	**Validation**	**Test**	**Validation**
RX10mm										
BCSD	**0.87(1.10)**	0.91(1.12)	0.85(4.61)	**0.90(2.38)**	0.90(2.39)	0.82(2.12)	**0.97(2.56)**	**0.96(1.93)**	**0.94**(2.54)	**0.93(2.21)**
EDA	0.85(0.83)	**0.93(0.86)**‡	**0.93(2.53)**‡	0.90(2.64)	**0.92**(2.62)†	**0.87**(2.19)‡	0.93(2.33)	0.91(1.92)	0.90(2.23)†	0.88(1.48)
EDA_PR	0.80(1.40)	0.90(1.68)	0.89(7.49)	0.81(6.98)	0.86(6.46)	0.77(4.47)	0.94(3.91)	0.93(2.97)	0.91(3.47)	0.85(2.83)
CDD										
BCSD	0.72(4.37)	0.85(4.37)	0.56(5.70)	0.57(5.70)	0.68(5.42)	**0.67**(6.07)	0.88(8.73)	0.88(5.55)	0.79(6.61)	0.78(7.27)
EDA	**0.77(2.67)**	**0.88(2.90)**	0.57(4.33)†	**0.71(4.15)**†	**0.76(4.20)**†	0.60(3.83)†	**0.92(6.07)**†	**0.88(4.10)**†	**0.83(4.96)**	**0.81(5.20)**†
EDA_PR	0.65(3.67)	0.85(3.29)	**0.60**(5.05)	0.61(5.06)†	0.61(4.62)	0.63(3.81)†	0.86(7.55)†	0.83(4.85)†	0.75(5.88)	0.76(5.83)
RX1day										
BCSD	0.83(11.76)	0.91(8.73)	**0.87**(39.59)	0.70(60.16)	0.85(37.54)	**0.90(42.64)**	**0.89(20.17)**	0.86(28.85)	**0.85**(19.04)	0.82(12.61)
EDA	**0.90(6.78)**†	**0.92(6.23)**†	0.84(37.87)†	**0.84(38.99)**†	**0.87(36.26)**	0.83(57.23)	0.88(19.52)†	**0.86(27.97)**	0.76(12.19)†	**0.82(6.63)**†
EDA_PR	0.77(15.17)	0.86(14.17)	0.75(61.19)	0.67(86.92)	0.78(66.28)	0.74(83.55)	0.82(26.83)	0.66(49.52)	0.70(20.75)	0.77(14.54)

Note: All the metrics are compared with the 5-km grids of the TCCIP observational rainfall. A superscript (†) indicates that the corresponding downscaling method performs significantly better than BCSD in CORR or RMSE at the 95% confidence level ($p < 0.05$). Bold and underlined values indicate the highest correlation coefficient among the downscaling methods. Underlined values indicate the lowest RMSE.

10970088, 2026, 0, Downloaded from https://rmets.onlinelibrary.wiley.com/doi/10.1002/joc.70607. By Statens Beredning, Wiley Online Library on [20/10/2026]. See the Terms and Conditions (https://onlinelibrary.wiley.com/terms-and-conditions) on Wiley Online Library for rules of use; OA articles are governed by the applicable Creative Commons License

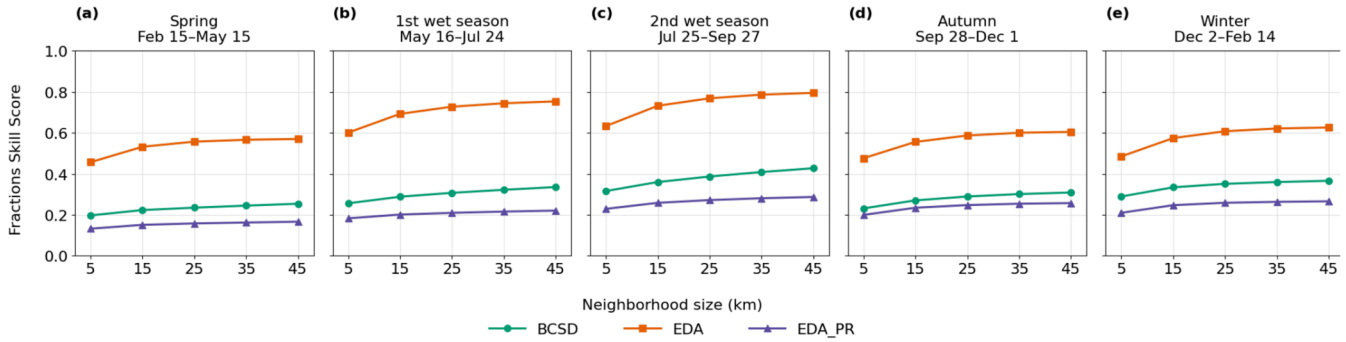

FIGURE 7 | Seasonal means of Fractions Skill Score (FSS) for daily rainfall exceeding 10 mm/day as a function of neighbourhood size during (a) spring, (b) the first wet season, (c) the second wet season, (d) autumn, and (e) winter. FSS was calculated relative to TCCIP for BCSD, EDA, and EDA_PR using neighbourhood sizes of 5–45 km. The plotted values are seasonal means of daily FSS, with larger values indicating better spatial agreement with the observed rainfall occurrence. [Colour figure can be viewed at wileyonlinelibrary.com]

TABLE 5 | Seasonal Structure–Amplitude–Location (SAL) verification of daily rainfall exceeding 10 mm/day for BCSD, EDA, and EDA_PR relative to TCCIP.

|S|/|A|/L	Spring	First-wet	Second-wet	Fall	Winter
10 mm					
BCSD	0.71/1.11/0.24	0.67/0.80/0.26	0.62/0.64/0.27	0.68/0.96/0.28	0.64/0.94/0.27
EDA	**0.30**†**/0.56**†**/0.08**†	**0.29**†**/0.36**†**/0.08**†	**0.30**†**/0.34**†**/0.09**†	**0.34**†**/0.57**†**/0.06**†	**0.32**†**/0.57**†**/0.07**†
EDA_PR	0.75/1.02/0.22	0.78/0.95/0.22	0.66/0.82/0.22	0.65/0.99/0.20	0.63/0.95/0.19

Note: Each entry reports the seasonal mean absolute Structure error (|S|), absolute Amplitude error (|A|), and Location error (L) in the format |S|/|A|/L, where smaller values indicate better agreement with the observed rainfall objects. Bold values indicate the lowest error among the three downscaling methods for each SAL component within a season. A superscript † denotes that the best-performing method is significantly better than both competing methods according to the paired bootstrap test at the 95% confidence level.

rainfall but also the morphology and organization of rainfall objects.

Together, the FSS and SAL analyses provide complementary evidence that the proposed EDA framework improves the spatial representation of daily rainfall. While FSS demonstrates enhanced neighbourhoods-scale agreement, SAL indicates that the improvements are associated with more accurate rainfall-object intensity, structure, and spatial location. These results suggest that incorporating surface wind information helps the model better reproduce the observed spatial organization of rainfall events. The complete FSS results for the 1 and 50 mm/day thresholds and the corresponding SAL analyses are provided in Figure S3 and Table S2.

3.4 | Comparison With Rainfall Statistics of CWA Local Stations

The Central Weather Administration (CWA) of Taiwan operates an extensive network of observation stations across the island, situated in densely populated areas and critical topographical points. Here, we focus on station-scale performance during the two summer wet seasons, which are recognized as the most challenging periods for statistical downscaling due to complex convective and orographic interactions. As illustrated in the seasonal mean rainfall maps of Figure 1c, the three selected CWA stations—Tainan (22.9° N, 120.2° E), Taichung (24.15° N, 120.6° E), and Alishan (23.5° N, 120.8° E)—are strategically located within the primary rainfall hotspots that dominate Taiwan's summer climate. Tainan and Taichung, located in southern and central Taiwan respectively, represent two urban cities on the plains, whereas Alishan is positioned on mountain slopes at an elevation of 1500 m, providing insights into the impact of elevation on rainfall patterns. This selection provides critical insights into the impact of elevation and orographic enhancement on rainfall patterns—regimes where reanalysis products like ERA5 typically exhibit significant systematic biases. During the first wet season of summer, our analysis highlights a consistent issue with the ERA5 reanalysis: the overprediction of low-intensity rainfall events (less than 5 mm/day) across all stations (Figure 8a,b). This pattern illustrates the constraints of coarse-resolution models like ERA5, which tend to miss capturing extreme rainfall events and favor the forecasting of more frequent, yet milder, rainfall. In contrast, the EDA model shows considerable improvement in mitigating this bias for overly frequent, weak rainfall (under 5 mm/day). Additionally, the EDA model more accurately adjusts for heavy rainfall events (over 50 mm/day), especially at the Alishan station, a location significantly influenced by orographic rainfall. Here, the EDA model's performance is notably superior compared to the other stations.

For the second wet season, rainfall distribution among the urban stations, Tainan and Taichung, becomes more consistent, yet the EDA model maintains its precision in correcting both low (< 5 mm/day) and high (> 50 mm/day) rainfall categories (Figure 8a,b). Like in the first wet season, the EDA

10970088, 2026, 0, Downloaded from https://rmets.onlinelibrary.wiley.com/doi/10.1002/joc.70607. By Statens Beredning, Wiley Online Library on [20/10/2026]. See the Terms and Conditions (https://onlinelibrary.wiley.com/terms-and-conditions) on Wiley Online Library for rules of use; OA articles are governed by the applicable Creative Commons License

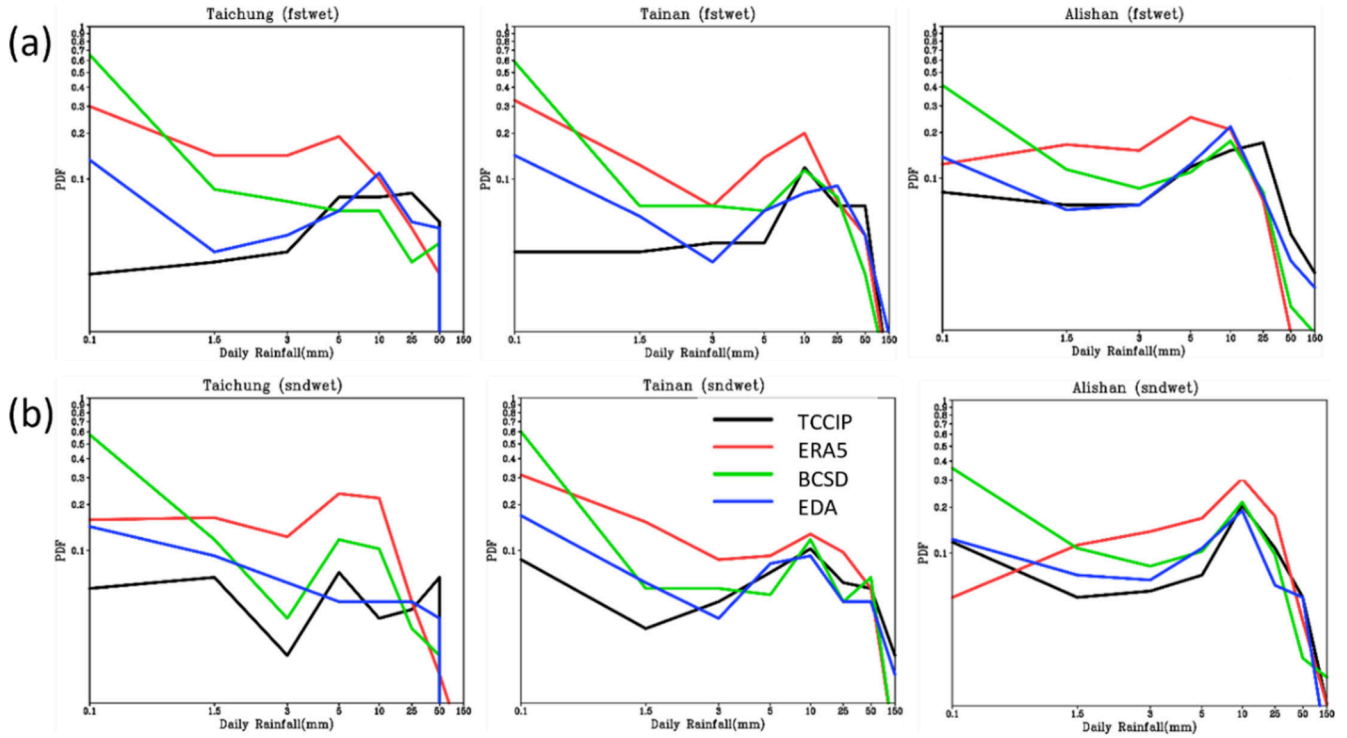

FIGURE 8 | Rainfall distribution for selected Central Weather Administration (CWA) observational stations during (a) the first wet season and (b) the second wet season. For the summer seasons, stations located on the western plains and mountains, including Tainan Station, Taichung Station, and Alishan Station, are featured. The arrangement of the stations in the figure follows a north-to-south order, based on the latitudinal positions of their locations, with stations positioned from top to bottom accordingly (Figure 1a). [Colour figure can be viewed at wileyonlinelibrary.com]

model's corrections are particularly effective at the Alishan station, successfully addressing the wet bias noted in the ERA5 reanalysis. On the other hand, the BCSD method tends to excel in adjusting rainfall within the mid-range spectrum, around 10 mm/day, accurately reflecting the average rainfall percentile for all three stations. However, it tends to overestimate the frequency of weak rainfall events even with correction from ERA5 statistics.

In summary, while the BCSD method more effectively adjusts mid-range rainfall amounts at the selected stations, the EDA model more consistently improves the representation of both low and high rainfall events at these sites. These results suggest that EDA can better capture rainfall variability across the sampled elevation and terrain settings, while the broader island-wide rainfall features should be interpreted together with analysis in other sections.

3.5 | Interannual Variations of Mean Rainfall and Rainfall Extremes

We examined the interannual variation in mean rainfall and extreme indices for the summer seasons, utilizing data from TCCIP, ERA5, BCSD, and the EDA model, as depicted in Figure 9. Our analysis, spanning from 2015 to 2020, includes both testing and validation phases. In the first wet season, TCCIP observations identify two significant peaks in mean rainfall for 2017 and 2019, which are not detected by the ERA5 reanalysis. This lack of detection in ERA5 is mirrored in the BCSD method, displaying a similar downward trend in both mean rainfall and the RX1day index (Figure 9a,b). However, when ERA5 does capture variations in the RX10mm and CDD indices, BCSD shows interannual variation alignment with TCCIP data (Figure 9c,d). Conversely, the EDA model more faithfully represents the interannual variability observed in the TCCIP dataset, covering both mean rainfall and extreme rainfall indices (Figure 9d). During the second wet season, characterized by typhoon-induced rainfall, ERA5 more accurately reflects the interannual changes in island-wide mean rainfall, resulting in comparable performance between EDA and BCSD (Figure 9a,c). Notably, the EDA model is better in portraying days of CDD more accurately than BCSD, which tends to underestimate the total count of CDD days significantly (Figure 9d). This superior performance of the EDA model is corroborated by correlation and RMSE metrics presented in Table 4 and aligns with rainfall statistics depicted in Figure 8. In essence, the EDA model provides a more precise depiction of interannual rainfall variations and extreme indices, particularly in correcting the misrepresented variability during the first wet Meiyu season by ERA5. It matches the BCSD model in capturing rainfall extremes and offers a more accurate distribution of CDD, thereby enhancing the model's ability to predict a wide range of rainfall and drought patterns accurately.

3.6 | Extreme Rainfall Event Cases During 2018–2020

We selected three extreme rainfall events characterized by the highest island-wide daily rainfall occurrences to evaluate the

10970088, 2026, 0, Downloaded from https://rmets.onlinelibrary.wiley.com/doi/10.1002/joc.70607. By Statens Beredning, Wiley Online Library on [20/10/2026]. See the Terms and Conditions (https://onlinelibrary.wiley.com/terms-and-conditions) on Wiley Online Library for rules of use; OA articles are governed by the applicable Creative Commons License

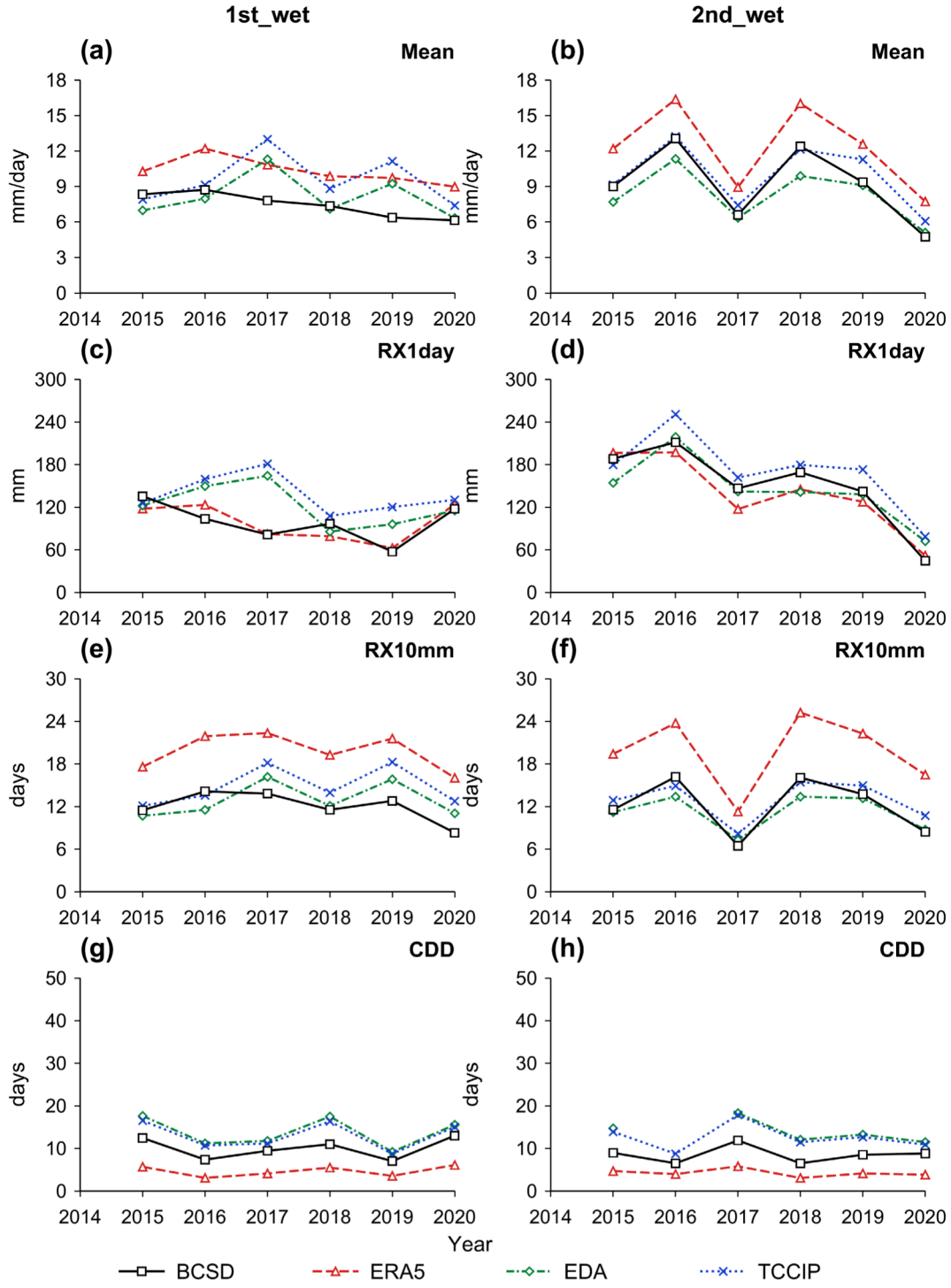

FIGURE 9 | Interannual variation of island-wide mean rainfall and selected extreme indices based on TCCIP observations (blue), ERA5 (red), and EDA (green), and BCSD (black) for the (a, b) mean, (c, d) RX1day, (e, f) RX10mm, and (g, h) CDD indices. From left to right, columns indicate the first wet season and the second wet seasons during validation and test period. [Colour figure can be viewed at wileyonlinelibrary.com]

EDA model's ability to capture the extreme rainfall events. Figure 10 illustrates these rainfall events during the test period from 2018 to 2020. The first event, on May 22, 2020, saw intense rainfall up to 500 mm/day on the southwest side of Taiwan (Figure 10a). This event resulted from multi-scaled interactions involving a strong south-westerly monsoon flow, a southwest vortex, and a potent Meiyu front, which collectively triggered heavy rainfall on the windward slope of the Central Mountain (Chien and Chiu 2023, 2024). While the ERA5 reanalysis depicted a relatively uniform rainfall distribution across Taiwan with a magnitude of only 100 mm/day (Figure 10b), both BCSD and EDA accurately identified the rainfall peak at the southern tip of the Xue Mountains, with EDA pinpointing the maximum around 22.5° N but overestimating the intensity to 600 mm/day compared to the observed 500 mm/day (Figure 10c,d).

10970088, 2026, 0, Downloaded from https://rmets.onlinelibrary.wiley.com/doi/10.1002/joc.70607. By Statens Beredning, Wiley Online Library on [20/10/2026]. See the Terms and Conditions (https://onlinelibrary.wiley.com/terms-and-conditions) on Wiley Online Library for rules of use; OA articles are governed by the applicable Creative Commons License

The second significant rainfall event occurred on August 23 and 24, 2018, linked to a tropical depression, as depicted in the second and third panels of Figure 10. This system made landfall in southern Taiwan on August 23 and proceeded to the Taiwan Strait by August 24; a movement observed in the ERA5 reanalysis surface circulations (Figure 10b). The depression's interaction with the existing strong south-westerly flow resulted in enhanced moisture transport into southwestern Taiwan, focusing heavy rainfall on the windward slopes of Ali Mountain and the Central Mountain, where rainfall peaks reached up to 300 mm/day (Figure 10a; National Science and Technology Center for Disaster Reduction 2019). A key difference in the rainfall downscaled by the two models is evident in BCSD's adherence to the coarse resolution of ERA5, which fails to capture the spatial variability characteristic of extreme rainfall events (Figure 10b,c). Notably, BCSD mimics ERA5 reanalysis by generating increased rainfall over central Taiwan (~24° N) on both days and weaker rainfall on August 24 over southwestern Taiwan (Figure 10c). In contrast, the EDA model more accurately delineates the rain-affected regions in alignment with the

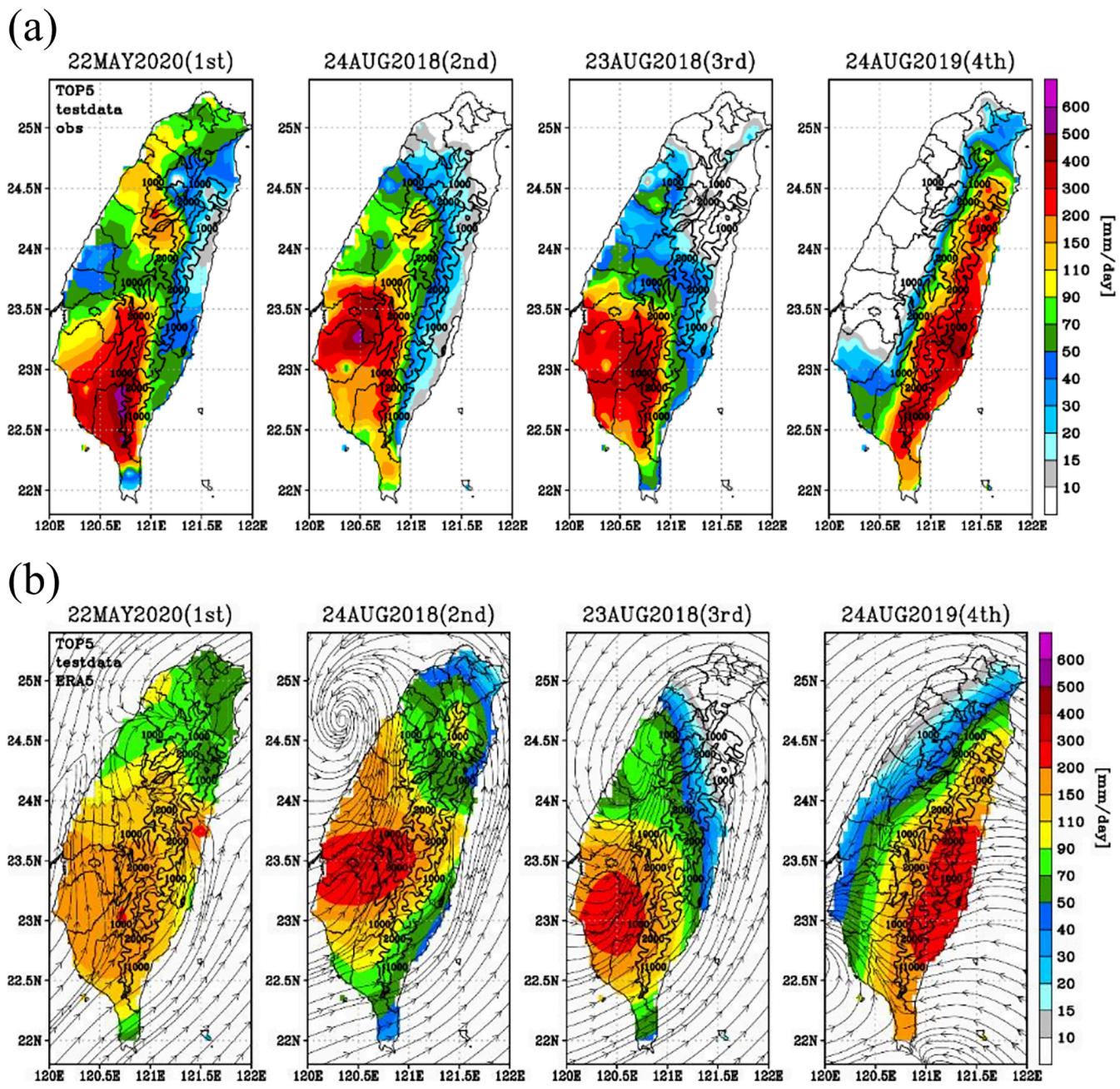

FIGURE 10 | Daily rainfall distributions for 4 days drawn from three extreme rainfall events identified from TCCIP during the test period (December 13, 2017 to December 31, 2020). The 4 days were selected from the highest island-wide daily mean rainfall days during this period. From left to right, they are May 22, 2020, August 24, 2018, August 23, 2018, and August 24, 2019. From the synoptic analysis of these rainfall days shows the May 22, 2020 event is related to a Meiyu frontal system, the event of August 23–24, 2018 is related to a tropical low-pressure system, and August 24, 2019 is related to Typhoon Bailu: (a) for TCCIP data set, (b) for ERA5 reanalysis, (c) BCSD downscaling method, and (d) for EDA downscaling model. Elevation contours at 1000 and 2000 m are represented by thick black lines, and the boundaries of each county in Taiwan are depicted with fine black lines. [Colour figure can be viewed at wileyonlinelibrary.com]

10970088, 2026, 0, Downloaded from https://rmets.onlinelibrary.wiley.com/doi/10.1002/joc.70607. By Statens Beredning, Wiley Online Library on [20/10/2026]. See the Terms and Conditions (https://onlinelibrary.wiley.com/terms-and-conditions) on Wiley Online Library for rules of use; OA articles are governed by the applicable Creative Commons License

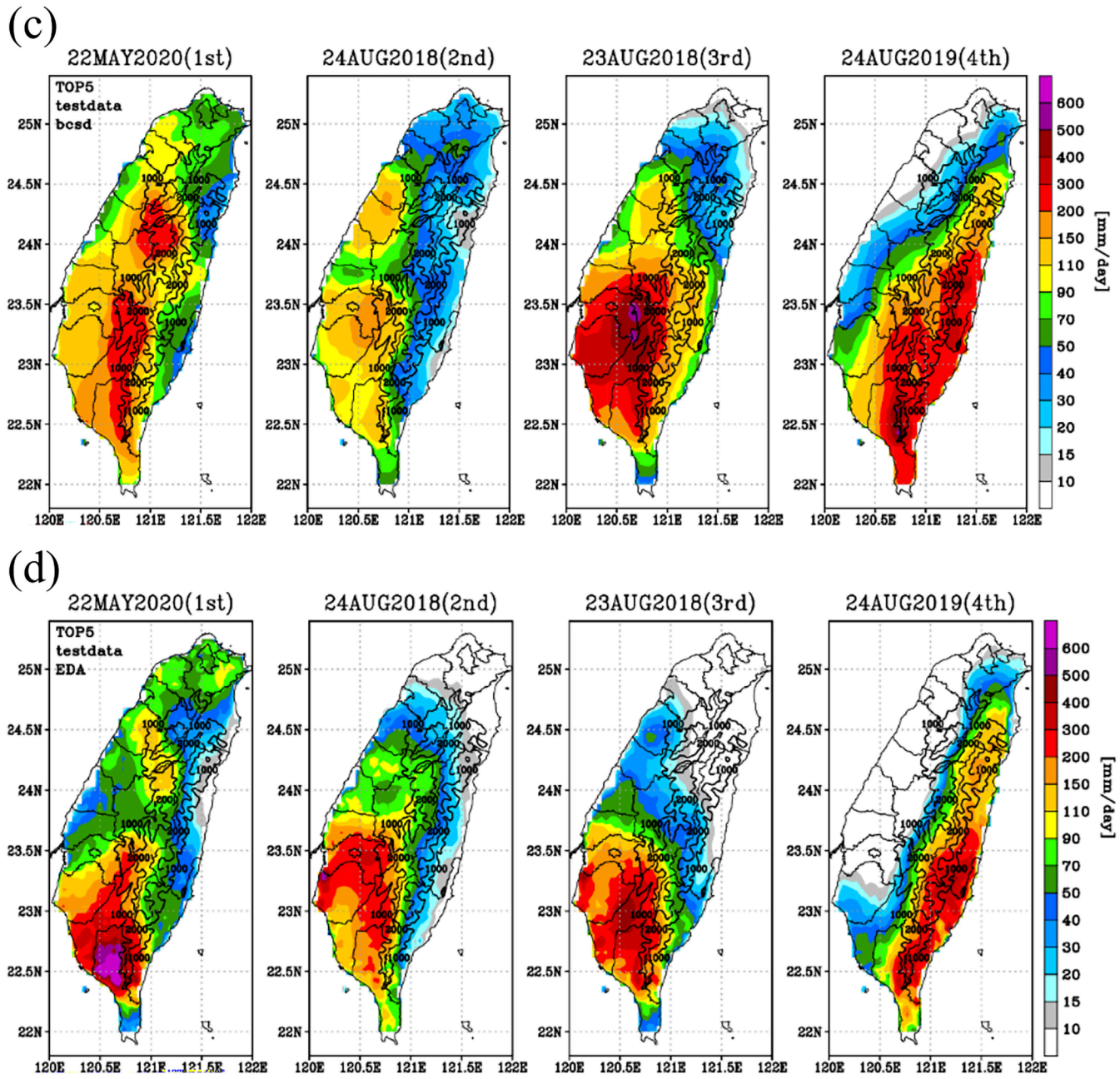

FIGURE 10 | (Continued)

topography for both days, offering a clearer north–south differentiation between dry and wet areas.

The third event, occurring on August 24, 2019, involved the severe tropical storm Bailu making a brief landfall at the southern tip of Taiwan before moving toward the Taiwan Strait. This event resulted in significant rainfall across the eastern part of the Central Mountain as Bailu (2019) approached (the 4th panel of Figure 10a). ERA5 reanalysis captured the rainfall on the eastern side of the Central Mountain as the storm neared but tended to overestimate rainfall on the western slope of the Central Mountain and Ali Mountain, likely due to its coarse resolution (Figure 10b). This overestimation by ERA5 was similarly reflected in the BCSD model, which inaccurately extended rainfall coverage too far westward, encroaching into the southern part of the Central Mountain area (Figure 10c). Conversely, the EDA model delineated the precise boundaries of the windward rainfall events, offering a more accurate representation of the interactions between the storm's dynamics and Taiwan's topography (Figure 10d). However, upon closer examination, the EDA model's rainfall pattern appears smoother compared to the TCCIP rainfall, indicating a limitation in capturing the localized, cell-like structures of rainfall, particularly on the northeastern part of Taiwan (Figure 10d).

To provide an initial qualitative assessment of the learned spatial representations, we examined the Transformer attention maps for the representative Meiyu event on May 22, 2020 (Section S3). For this event, the attention maps exhibit structured spatial patterns rather than random distributions (Figure S4). Different attention heads focus on complementary regions, while deeper encoder layers develop broader spatial dependencies across

10970088, 2026, 0, Downloaded from https://rmets.onlinelibrary.wiley.com/doi/10.1002/joc.70607. By Statens Beredning, Wiley Online Library on [20/10/2026]. See the Terms and Conditions (https://onlinelibrary.wiley.com/terms-and-conditions) on Wiley Online Library for rules of use; OA articles are governed by the applicable Creative Commons License

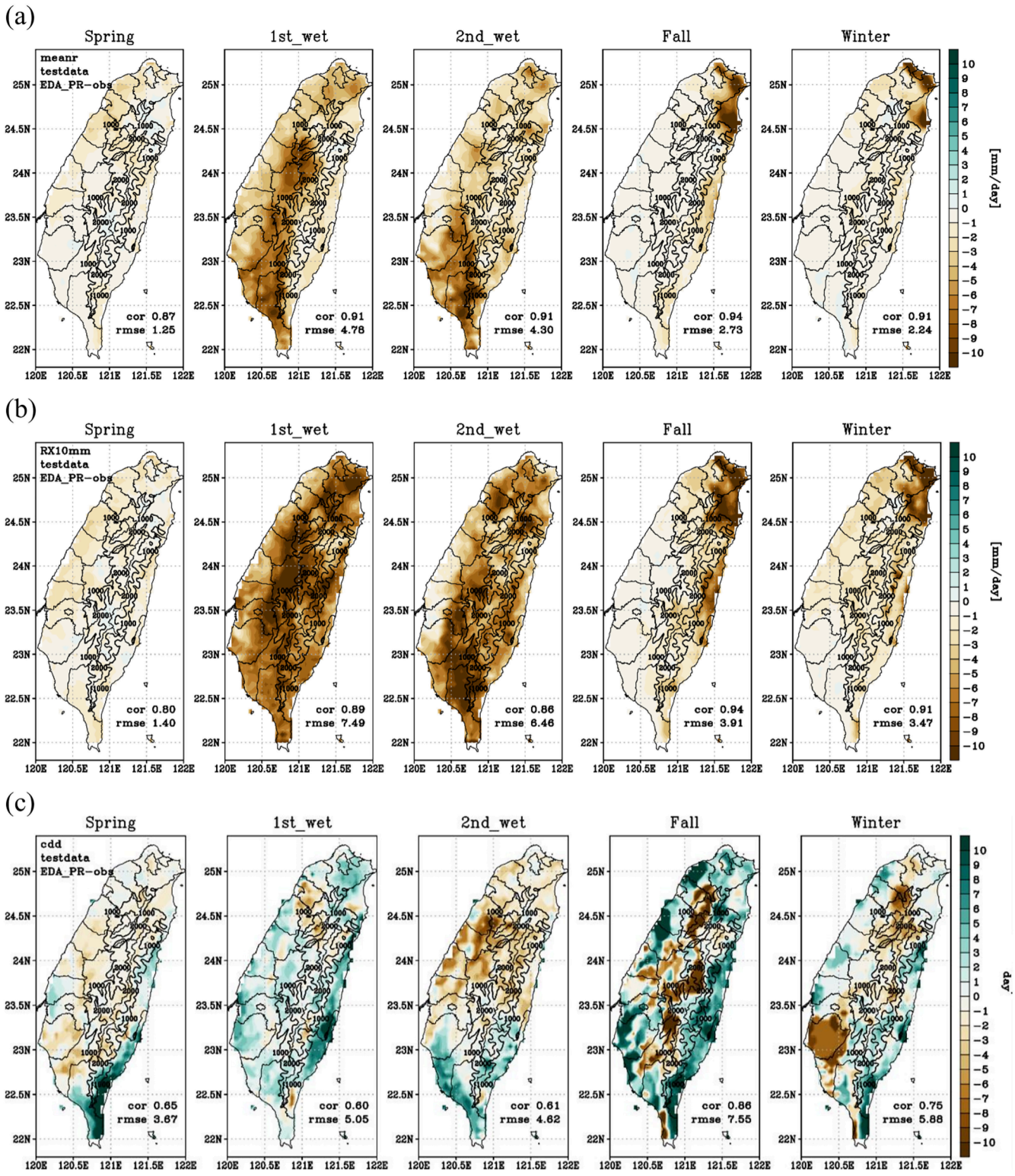

FIGURE 11 | Spatial distribution of downscaled rainfall based on EDA model structure but with only rainfall as the input for 5 rainy seasons in Taiwan. (a) Mean rainfall, (b) RX10mm, and (c) CDD difference from TCCIP during test period (December 13, 2017 to December 31, 2020). [Colour figure can be viewed at wileyonlinelibrary.com]

Taiwan. These observations suggest that the model integrates information from multiple surrounding locations when generating rainfall predictions. We emphasize, however, that this analysis is limited to one representative event and serves only as an illustrative example. A systematic investigation across multiple events and weather regimes is left for future work.

In summary, the EDA model shows improved performance in reproducing the selected extreme rainfall events, particularly for cases influenced by interactions between topography and synoptic circulation. Together with the seasonal-scale results, these case studies suggest that the model can better represent certain terrain-influenced rainfall patterns, although this

10970088, 2026, 0, Downloaded from https://rmets.onlinelibrary.wiley.com/doi/10.1002/joc.70607. By Statens Beredning, Wiley Online Library on [20/10/2026]. See the Terms and Conditions (https://onlinelibrary.wiley.com/terms-and-conditions) on Wiley Online Library for rules of use; OA articles are governed by the applicable Creative Commons License

evidence should be interpreted as event-based and qualitative rather than as a comprehensive demonstration across all extreme-event types.

3.7 | Surface-Wind Ablation: EDA Versus EDA_PR

To isolate the role of near-surface flow, we ran an ablation experiment in which EDA_PR uses rainfall only, whereas the full EDA uses rainfall plus surface wind. This setup tests whether low-level circulation is needed to recover orographic rainfall structure. Figure 11 and Tables 3 and 4 show that, relative to EDA, EDA_PR underestimates mean rainfall on windward slopes and weakens RX10mm and CDD skill. The loss of skill indicates that surface wind is needed to reproduce rainfall maxima, event persistence, and terrain-controlled dry-day patterns. Taken together, the ablation suggests that the performance of EDA benefits from incorporating physically meaningful predictors: surface winds help reproduce rainfall patterns associated with monsoonal flow interacting with topography, especially in windward rainfall hotspots.

4 | Discussion

4.1 | Interpretation of EDA Improvements

Our study underscores the capability and potential of the DL-based model, the EDA, to enhance univariate rainfall downscaling, specifically in accurately transitioning coarse-resolution rainfall data to a finer, local-scale resolution by incorporating auxiliary topographical and surface circulation data. By utilizing the ERA5 reanalysis as input, our primary focus was on mitigating the biases associated with orographic rainfall, a common challenge arising from the limited resolution and parameterization of global models. Taiwan, with its extensive network of rainfall observations and a diverse climate characterized by significant orographic influence on precipitation patterns, offered an ideal setting for this study. This choice allowed for a thorough assessment of the EDA model's capacity from both seasonal mean, extreme indices, and individual extreme events to downscale and maintain variability in daily rainfall data, which are particularly important in regions with complex climatic and topographical dynamics, like Taiwan.

Our comprehensive analysis, encompassing evaluations of seasonal rainfall, ETCCDI extreme indices, and their internal variations, underscores the EDA model's proficiency in correcting rainfall biases from the ERA5 reanalysis across various seasons. Its performance, in terms of correlation (CORR) and root mean square error (RMSE) across seasonal rainfall and climate extreme index patterns, is on par with that of the BCSD method, especially in the seasonal mean pattern. Upon closer examination, however, the EDA model exhibits superior capabilities in amending the overly frequent occurrences of weak rainfall and in accurately addressing instances of heavy rainfall identified in the TCCIP observations, outperforming the BCSD method in these respects. This enhanced performance is particularly notable during the first and second wet seasons in Taiwan, characterized by extreme rainfall events. The EDA model's improved adjustments are evident in climate extreme indices that capture both ends of the rainfall spectrum, such as CDD and rainfall exceeding 10 mm (RX10mm). Additionally, the EDA model surpasses the BCSD method in predicting interannual variations of seasonal rainfall and climate extremes, areas where the BCSD method struggles, especially when the parent ERA5 data inaccurately represents rainfall variability.

4.2 | Relation to Previous Work

Traditional statistical downscaling methods such as BCSD remain attractive because of their computational efficiency and robust performance in reproducing large-scale climatological statistics. However, previous comparative studies have shown that no single downscaling method consistently outperforms others across different regions and climate regimes, particularly over areas with complex terrain where precipitation is governed by multiple interacting physical processes (e.g., Chen et al. 2010; Themeßl et al. 2012; Jaiswal et al. 2022; Tiwari and Garg 2025). Consistent with these findings, our results indicate that the primary advantages of the EDA model are found in reproducing heavy rainfall, climate extremes, and interannual variability, while maintaining performance comparable to BCSD for seasonal mean rainfall. These improvements are particularly evident during Taiwan's wet seasons, when precipitation is strongly influenced by interactions among monsoon circulation, tropical cyclones, mesoscale convection, and steep topography. Our research sets itself apart by deploying a DL model tailored to Taiwan's distinct climate characteristics, marked by its intricate weather systems and pronounced topographical impact on rainfall distribution. This approach proves effective in addressing the limitations associated with QM-type methods, such as the artificial adjustment of rainfall extremes and inaccuracies in rainfall location due to complex terrain (Maraun and Widmann 2018). Our application of a DL model for downscaling not only validates the effectiveness of DL models in refining downscaling methods for climate purposes but also underscores their flexibility to incorporate auxiliary data. Our analysis of rainfall pattern and statistics shows that this inclusion is crucial for representing the intricate rainfall pattern determined by dynamics between topography and atmospheric circulations.

While Chiang et al. (2024) established the feasibility of DL structure for daily precipitation downscaling over Taiwan, the present study advances this line of research by extending the framework to climate downscaling applications, incorporating methodological improvements, and evaluating its ability to reproduce climate-related context. Parallel to our focus on climate downscaling, Hsu et al. (2024) found that a CNN-based model excels in amending rainfall patterns for weather forecast datasets on a subdaily basis across Taiwan. Moreover, Mardani et al. (2025) showcased the effectiveness of combining U-net with a diffusion model for enhancing the downscaling of kilometre-scale surface variables in Taiwan, mimicking the output of data-assimilated regional models. In contrast, our study focuses on climate downscaling, where preserving seasonal climatology, rainfall extremes, and interannual variability is equally important. This distinction requires evaluation beyond conventional accuracy

10970088, 2026, 0, Downloaded from https://rmets.onlinelibrary.wiley.com/doi/10.1002/joc.70607. By Statens Beredning, Wiley Online Library on [20/10/2026]. See the Terms and Conditions (https://onlinelibrary.wiley.com/terms-and-conditions) on Wiley Online Library for rules of use; OA articles are governed by the applicable Creative Commons License

metrics and highlights the importance of assessing physically meaningful climate statistics.

4.3 | Comparison With a Standard U-Net Baseline

To further evaluate whether the improvements of the proposed EDA framework arise from its architectural design rather than the application of deep learning alone, we additionally compared EDA with a standard U-Net architecture (Ronneberger et al. 2015) trained using the same training, validation, and testing datasets. The U-Net contains approximately 1.75 million trainable parameters, which is comparable to the proposed EDA model, providing a fair comparison between the two deep learning approaches. The complete quantitative and spatial evaluations are presented in Table S1 and Figures S1 and S2.

Overall, the U-Net provides a strong deep learning baseline and successfully reproduces the broad spatial characteristics of seasonal rainfall and extreme precipitation. However, EDA generally achieves higher spatial correlations and lower RMSE for seasonal rainfall climatology and several extreme rainfall indices (Table S1). The seasonal RX1day maps (Figure S1) indicate that both models capture the large-scale spatial distribution of heavy rainfall, while EDA better reproduces localized maxima over Taiwan's complex terrain. Similarly, the four representative extreme rainfall events (Figure S2) demonstrate that both models successfully identify the locations of major rainfall systems, whereas EDA generally preserves finer-scale rainfall structures and terrain-induced precipitation more effectively. These results suggest that the proposed EDA framework, which integrates attention mechanisms with physically relevant surface wind information, provides additional benefits over a conventional encoder–decoder CNN for rainfall downscaling in regions with complex topography.

4.4 | Limitations

Several limitations of this study should be acknowledged. First, the training, validation, and testing periods sample different meteorological conditions, particularly with respect to the strong interannual variation of typhoon trajectories and storm characteristics over Taiwan. As a result, the second wet season presents a greater challenge because some typhoon scenarios are underrepresented in the training dataset. This sampling discrepancy is most evident for rainfall extremes, where the CORR and RMSE of extreme indices exhibit larger variations than those of seasonal mean rainfall. These results suggest that capturing the diversity of extreme rainfall events, particularly typhoon-induced rainfall, may require larger and more diverse training datasets, improved sampling strategies, or probabilistic and generative downscaling frameworks capable of representing multiple plausible realizations of extreme precipitation.

Second, the proposed framework is subject to uncertainties associated with both the training data and the deep learning model itself. The reference TCCIP gridded rainfall dataset is generated through interpolation of station observations and is therefore affected by uncertainties related to station density, interpolation methodology, and the representation of rainfall over complex terrain. Likewise, ERA5 reanalysis contains uncertainties in representing precipitation and atmospheric circulation over mountainous regions. These uncertainties propagate into both model training and evaluation and should be considered when interpreting the reported model performance, particularly for climate impact applications. In the meantime, the current EDA framework introduces model uncertainty. The model produces a single deterministic realization for each input and has been evaluated using one optimized model configuration. Consequently, uncertainties associated with random initialization, training stochasticity, hyperparameter selection, and architectural choices have not been explicitly quantified. Future work should investigate the robustness of the framework through ensemble training, multiple random initializations, or Bayesian and probabilistic deep learning approaches.

Also, despite the improved representation of heavy rainfall, the model still tends to underestimate the most extreme precipitation events. This limitation is primarily attributable to the rarity of such events in the training dataset, which makes it difficult for supervised learning to adequately constrain the nonlinear relationships associated with the upper tail of the rainfall distribution. Furthermore, extreme rainfall over Taiwan is often controlled by highly localized convective processes, terrain–atmosphere interactions, and tropical cyclones, resulting in substantial spatial variability that is challenging for deterministic regression models to reproduce. As shown in Figure 1b, typhoon-related rainfall contributes disproportionately to the most extreme precipitation events and represents a major source of interannual rainfall variability over Taiwan. Consequently, even small uncertainties in storm track, translation speed, or large-scale atmospheric conditions can lead to considerable differences in localized rainfall. Although the weighted loss function alleviates this issue by assigning greater importance to heavy rainfall during training, accurately representing the most extreme events remains an open challenge. Future work may benefit from larger training datasets, specialized extreme-event sampling strategies, and hybrid dynamical–statistical, probabilistic, or generative frameworks that can better represent the uncertainty associated with rare precipitation extremes.

Finally, the transferability of the trained model to future climate conditions remains an open question. The EDA model is trained using historical ERA5 rainfall and surface wind fields and therefore assumes that the statistical relationships between the auxiliary predictors and rainfall remain sufficiently stable under changing climate conditions. As with other statistical and deep learning-based downscaling methods, these relationships may become less reliable when future climate states fall outside the range represented in the training data. Although the incorporation of physically informed predictors may improve model generalization, dedicated evaluation using CMIP6-driven simulations will be necessary to assess the robustness of the framework under future climate conditions. In addition, approaches such as domain adaptation and transfer learning may help improve transferability across climate regimes and warrant further investigation.

4.5 | Future Directions

Our future research works are oriented along two primary trajectories. First, we aim to leverage our comprehensive

10970088, 2026, 0, Downloaded from https://rmets.onlinelibrary.wiley.com/doi/10.1002/joc.70607. By Statens Beredning, Wiley Online Library on [20/10/2026]. See the Terms and Conditions (https://onlinelibrary.wiley.com/terms-and-conditions) on Wiley Online Library for rules of use; OA articles are governed by the applicable Creative Commons License

understanding of Taiwan's rainy seasons, derived from detailed observational analyses, to refine the identification of rainfall characteristics most accurately captured by the EDA model. As an initial step in this direction of explainability, we performed a qualitative attention-map analysis for a representative Meiyu event (Section S3), which illustrates how the Transformer encoder integrates spatial information for rainfall prediction. However, this analysis is limited to a single representative case and provides only qualitative insight into the learned spatial representations. Future work should extend this preliminary analysis by systematically investigating attention patterns across multiple weather regimes, representative events, output locations, and attention heads, together with complementary explainability techniques, to establish more robust links between the learned representations and physically meaningful atmospheric processes. Recent work by Chang et al. (2026), building upon the downscaling framework of Chiang et al. (2024), demonstrates how visual analytics can be used to uncover a certain climate concept that are distinguishable and used in downscaling work in DL models. More broadly, many studies have also emphasized the need for improved model transparency with interpretability approaches, which aim to relate learned model features to physically meaningful mechanisms, such as linking model responses to large-scale circulation patterns, thermodynamic conditions, and topographic influences (e.g., McGovern et al. 2019; Molina et al. 2023). These approaches provide valuable insights into how models represent key processes but are often tailored to specific applications and may not fully capture the full complexity of learned representations. Integrating these complementary approaches with attention-based analyses provides a promising pathway toward improving the physical interpretability and scientific credibility of deep learning-based climate downscaling models.

Second, we aim to extend the EDA framework to climate change applications, particularly using CMIP models. A central challenge in this extension lies in the selection of predictors and training strategy. While univariate approaches offer practical advantages—such as reduced data requirements and broader applicability across GCMs with limited variable availability—multivariate approaches have consistently demonstrated improved performance. In particular, emulator-type frameworks that incorporate multiple atmospheric predictors (e.g., Baño-Medina et al. 2020, 2021; Doury et al. 2023; Rampal et al. 2024, 2025) are widely employed in downscaling from GCMs to CORDEX-scale projections. However, a fundamental question remains unresolved: how many and which predictors are required to optimally constrain the model without inducing overfitting. In this context, univariate approaches offer a complementary advantage by reducing model complexity and enabling application across a broader range of datasets and GCMs. Moreover, critical challenges—including extrapolability to future climate regimes and robustness across different GCMs—must be rigorously evaluated prior to applying the EDA framework to CMIP-type simulations. Building on these considerations, we plan to apply the model to selected CMIP6 simulations to systematically assess its robustness, scalability, and generalizability across varying predictor configurations and forcing scenarios. Through this effort, we aim to advance the development of efficient and physically consistent data-driven downscaling methodologies and to enhance the reliability of local-scale climate projections for Taiwan.

5 | Conclusions

This study developed and evaluated the Encoder–Decoder with Multi-head Attention for Auxiliary channels (EDA), an attention-based deep learning model to reproduce 5-km TCCIP-based daily rainfall pattern from 25-km ERA5 inputs over Taiwan's complex terrain. By incorporating 10-m surface winds, coarsened precipitation, and topography as auxiliary predictors, together with a WMSE loss function, the model aims to improve the representation of terrain-controlled rainfall and reduce common deficiencies of coarse-resolution reanalysis, including spatial displacement and excessive weak rainfall.

Compared with the BCSD method, EDA more accurately reproduces the spatial distribution of seasonal rainfall, selected rainfall extremes (RX1day, RX10mm, and CDD), and interannual variability, with the largest improvements occurring during the Meiyu and typhoon-dominated summer seasons. In contrast, BCSD remains highly competitive during the relatively stable autumn and winter monsoon seasons, indicating that the advantages of EDA are greatest when rainfall is strongly influenced by circulation-topography interactions. The conclusions regarding rainfall extremes should, however, be interpreted in light of the relatively short 2018–2020 test period, which may not fully sample the range of interannual and typhoon-related variability over Taiwan.

The ablation experiment demonstrates that incorporating surface winds provides additional information beyond rainfall alone, leading to more realistic windward and leeward rainfall patterns over Taiwan's steep terrain. These improvements suggest that physically informed auxiliary predictors help the model better represent circulation-dependent rainfall distributions. Nevertheless, the model remains a statistical learning framework, and the results should be interpreted as an improved representation of physically meaningful relationships rather than direct learning of atmospheric processes.

Beyond demonstrating improved predictive skill, this study contributes to the growing body of deep-learning downscaling research by emphasizing physically informed predictor selection and climate-oriented evaluation. While previous studies have primarily focused on improving statistical accuracy or developing new neural network architectures, our results show that incorporating circulation-related information can enhance the representation of terrain-controlled rainfall processes and clarify the conditions under which deep learning provides added value over conventional statistical downscaling methods.

Overall, this study demonstrates the potential of physically informed deep learning to enhance statistical rainfall downscaling over regions with complex terrain. By integrating physically meaningful auxiliary predictors with a comprehensive climate-oriented evaluation, the proposed framework shows promise for producing higher-resolution gridded climate information to support hydrological applications, water resource management, and climate impact assessment in topographically complex regions.

10970088, 2026, 0, Downloaded from https://rmets.onlinelibrary.wiley.com/doi/10.1002/joc.70607. By Statens Beredning, Wiley Online Library on [20/10/2026]. See the Terms and Conditions (https://onlinelibrary.wiley.com/terms-and-conditions) on Wiley Online Library for rules of use; OA articles are governed by the applicable Creative Commons License

Author Contributions

Yi-Chi Wang: conceptualization, methodology, funding acquisition, project administration, supervision, writing – original draft, writing – review and editing. **Chia-Hao Chiang:** methodology, software, data curation, investigation, validation. **Chiung-Jui Su:** visualization, investigation. **Ko-Chih Wang:** conceptualization, writing – review and editing, supervision, project administration. **Wan-Ling Tseng:** conceptualization, writing – review and editing, project administration, funding acquisition. **Hsin-Chien Liang:** data curation.

Acknowledgements

We thank four anonymous reviewers for providing constructive and useful suggestions to help our work improve significantly. We thank Professor Cheng-Ta Chen (Department of Earth Sciences, National Taiwan Normal University, Taipei, Taiwan) for valuable discussions and insights that contributed to this study. We are also grateful to the National Center for High-Performance Computing of Taiwan for providing the facilities for model training, testing, and validation. The authors also acknowledge the support of Horizon Europe project Impetus for Change (I4C, grant nr. Grant Agreement 101081555).

Funding

This work was supported by the Taiwan National Council of Science and Technology under grant numbers 112-2923-M-001-003-MY4, 114-2628-M-007-007-MY4, 115-2111-M-003-006.

Conflicts of Interest

The authors declare no conflicts of interest.

Data Availability Statement

The exact version of the EDA, used to produce the results used in this paper, and scripts to run the model are archived on Zenodo (Chiang 2024a), as are output data to produce the plots for all the simulations presented in this paper (Chiang 2024b). The input data, TCCIP daily rainfall dataset, can be downloaded from the project website (https://tccip.ncdr.nat.gov.tw/index_eng.aspx), and the rainfall and surface variables from the ERA5 reanalysis can be downloaded from the Copernicus Climate Change Service (Hersbach et al. 2023).

References

Adewoyin, R. A., P. Dueben, P. Watson, Y. He, and R. Dutta. 2021. "TRU-NET: A Deep Learning Approach to High Resolution Prediction of Rainfall." *Machine Learning* 110: 2035–2062. https://doi.org/10.1007/s10994-021-06022-6.

Baño-Medina, J., R. Manzanas, and J. M. Gutiérrez. 2020. "Configuration and Intercomparison of Deep Learning Neural Models for Statistical Downscaling." *Geoscientific Model Development* 13: 2109–2124. https://doi.org/10.5194/gmd-13-2109-2020.

Baño-Medina, J., R. Manzanas, and J. M. Gutiérrez. 2021. "On the Suitability of Deep Convolutional Neural Networks for Continental-Wide Downscaling of Climate Change Projections." *Climate Dynamics* 57: 2941–2951. https://doi.org/10.1007/s00382-021-05847-0.

Bürger, G., S. R. Sobie, A. J. Cannon, A. T. Werner, and T. Q. Murdock. 2013. "Downscaling Extremes: An Intercomparison of Multiple Methods for Future Climate." *Journal of Climate* 26: 3429–3449. https://doi.org/10.1175/JCLI-D-12-00249.1.

Cannon, A. J., S. R. Sobie, and T. Q. Murdock. 2015. "Bias Correction of GCM Precipitation by Quantile Mapping: How Well Do Methods Preserve Changes in Quantiles and Extremes?" *Journal of Climate* 28: 6938–6959. https://doi.org/10.1175/JCLI-D-14-00754.1.

Chang, P. C., Z. H. Huang, W. L. Tseng, et al. 2026. "A Visual Analytics Approach to Exploring Regional Physical Processes Reflected in Generative Climate Downscaling Models." *Information Visualization* 25: 288–309. https://doi.org/10.1177/14738716261434910.

Chen, C.-S., and Y.-L. Chen. 2003. "The Rainfall Characteristics of Taiwan." *Monthly Weather Review* 131: 1323–1341. https://doi.org/10.1175/1520-0493(2003)131<1323:TRCOT>2.0.CO;2.

Chen, S.-C., P.-S. Yu, and Y.-H. Tang. 2010. "Statistical Downscaling of Daily Precipitation Using Support Vector Machines and Multivariate Analysis." *Journal of Hydrology* 385, no. 1–4: 13–22. https://doi.org/10.1016/j.jhydrol.2010.01.021.

Chiang, C.-H. 2024a. *EnDeAux_Climate_Downscaling [code]*. Zenodo. https://doi.org/10.5281/zenodo.10937920.

Chiang, C.-H. 2024b. *Simulation Datasets for Wang et al. (2024): Using Multi-Head Attention Deep Neural Network for Bias Correction and Downscaling for Daily Rainfall Pattern of a Subtropical Island [dataset]*. Zenodo. https://doi.org/10.5281/zenodo.10976853.

Chiang, C.-H., Z.-H. Huang, L. Liu, et al. 2024. "Climate Downscaling: A Deep-Learning-Based Super-Resolution Model of Precipitation Data With Attention Block and Skip Connections." *arXiv*. https://doi.org/10.48550/arXiv.2403.17847.

Chien, F.-C., and Y.-C. Chiu. 2023. "Factors Leading to Heavy Rainfall in Southern Taiwan in the Early Mei-Yu Season of 2020." *Monthly Weather Review* 151: 1885–1908. https://doi.org/10.1175/MWR-D-22-0226.1.

Chien, F.-C., and Y.-C. Chiu. 2024. "The Impact of Large-Scale Environments and a Southwest Vortex on Heavy Rainfall in Southern Taiwan in Late May 2020." *Monthly Weather Review* 152: 745–767. https://doi.org/10.1175/MWR-D-23-0198.1.

Chou, C., L. Huang, L. Tseng, J. Tu, and P. Tan. 2009. "Annual Cycle of Rainfall in the Western North Pacific and East Asian Sector." *Journal of Climate* 22: 2073–2094. https://doi.org/10.1175/2008JCLI2538.1.

Dong, C., C. C. Loy, K. He, and X. Tang. 2014. "Image Super-Resolution Using Deep Convolutional Networks." *arXiv Preprint*. arXiv:1501.00092. https://arxiv.org/abs/1501.00092.

Doury, A., S. Somot, S. Gadat, A. Ribes, and L. Corre. 2023. "Regional Climate Model Emulator Based on Deep Learning: Concept and First Evaluation of a Novel Hybrid Downscaling Approach." *Climate Dynamics* 60: 1751–1779. https://doi.org/10.1007/s00382-022-06343-9.

Frich, P., L. V. Alexander, P. Della-Marta, et al. 2002. "Observed Coherent Changes in Climatic Extremes During the Second Half of the Twentieth Century." *Climate Research* 19: 193–212.

Harris, L., A. T. T. McRae, M. Chantry, P. D. Dueben, and T. N. Palmer. 2022. "A Generative Deep Learning Approach to Stochastic Downscaling of Precipitation Forecasts." *Journal of Advances in Modeling Earth Systems* 14: e2022MS003120. https://doi.org/10.1029/2022MS003120.

Henny, L., C. D. Thorncroft, H. Hsu, and L. F. Bosart. 2023. "Changes in Extreme Precipitation in Taiwan's Mei-Yu Season." *Quarterly Journal of the Royal Meteorological Society* 149: 1810–1832. https://doi.org/10.1002/qj.4483.

Henny, L., C. D. Thorncroft, H.-H. Hsu, and L. F. Bosart. 2021. "Extreme Rainfall in Taiwan: Seasonal Statistics and Trends." *Journal of Climate* 34: 1–51. https://doi.org/10.1175/JCLI-D-20-0999.1.

Hersbach, H., B. Bell, P. Berrisford, et al. 2020. "The ERA5 Global Reanalysis." *Quarterly Journal of the Royal Meteorological Society* 146: 1999–2049. https://doi.org/10.1002/qj.3803.

Hersbach, H., B. Bell, P. Berrisford, et al. 2023. *ERA5 Hourly Data on Single Levels From 1940 to Present*. Copernicus Climate Change Service (C3S) Climate Data Store (CDS). https://doi.org/10.24381/cds.adbb2d47.

10970088, 2026, 0, Downloaded from https://rmets.onlinelibrary.wiley.com/doi/10.1002/joc.70607. By Statens Beredning, Wiley Online Library on [20/10/2026]. See the Terms and Conditions (https://onlinelibrary.wiley.com/terms-and-conditions) on Wiley Online Library for rules of use; OA articles are governed by the applicable Creative Commons License

Hsu, L.-H., c.-c. Chiang, K.-L. Lin, et al. 2024. "Downscaling Taiwan Precipitation With a Residual Deep Learning Approach." *Geoscience Letters* 11: 23. https://doi.org/10.1186/s40562-024-00340-y.

Jaiswal, R., R. K. Mall, N. Singh, et al. 2022. "Evaluation of Bias Correction Methods for Regional Climate Models: Downscaled Rainfall Analysis Over Diverse Agroclimatic Zones of India." *Earth and Space Science* 9. https://doi.org/10.1029/2021EA001981.

Karl, T. R., N. Nicholls, and A. Ghazi. 1999. "CLIVAR/GCOS/WMO Workshop on Indices and Indicators for Climate Extremes: Workshop Summary." *Climatic Change* 42: 3–7.

Kumar, B., R. Chattopadhyay, M. Singh, N. Chaudhari, K. Kodari, and A. Barve. 2021. "Deep Learning-Based Downscaling of Summer Monsoon Rainfall Data Over Indian Region." *Theoretical and Applied Climatology* 143: 1145–1156. https://doi.org/10.1007/s00704-020-03489-6.

LeCun, Y., Y. Bengio, and G. Hinton. 2015. "Deep Learning." *Nature* 521: 436–444. https://doi.org/10.1038/nature14539.

Lin, L.-Y., C.-T. Lin, Y.-M. Chen, C.-T. Cheng, H.-C. Li, and W.-B. Chen. 2022. "The Taiwan Climate Change Projection Information and Adaptation Knowledge Platform: A Decade of Climate Research." *Water* 14, no. 3: 358. https://doi.org/10.3390/w14030358.

Lin, S., Y.-S. Tung, and S. Lin. 2023. *Working Paper for Rainfall Statistical Downscaling With AR6 Models (Version 1.0)*. Taiwan Climate Change Projection Information and Adaptation Knowledge Platform.

Liu, Y., A. R. Ganguly, and J. Dy. 2020. "Climate Downscaling Using YNet: A Deep Convolutional Network With Skip Connections and Fusion." In *Proceedings of the 26th ACM SIGKDD International Conference on Knowledge Discovery & Data Mining*, 303–313. Association for Computing Machinery. https://doi.org/10.1145/3394486.3403366.

Maraun, D., T. G. Shepherd, M. Widmann, et al. 2017. "Towards Process-Informed Bias Correction of Climate Change Simulations." *Nature Climate Change* 7: 764–773. https://doi.org/10.1038/nclimate3418.

Maraun, D., F. Wetterhall, A. M. Ireson, et al. 2010. "Precipitation Downscaling Under Climate Change: Recent Developments to Bridge the Gap Between Dynamical Models and the End User." *Reviews of Geophysics* 48: RG3003. https://doi.org/10.1029/2009RG000314.

Maraun, D., and M. Widmann. 2015. "The Representation of Location by a Regional Climate Model in Complex Terrain." *Hydrology and Earth System Sciences* 19: 3449–3456. https://doi.org/10.5194/hess-19-3449-2015.

Maraun, D., and M. Widmann. 2018. *Statistical Downscaling and Bias Correction for Climate Research*. Cambridge University Press. https://doi.org/10.1017/9781107588783.

Mardani, M., N. Brenowitz, N. Brenowitz, et al. 2025. "Residual Corrective Diffusion Modeling for Km-Scale Atmospheric Downscaling." *Communications Earth & Environment* 6: 124. https://doi.org/10.1038/s43247-025-02042-5.

McGovern, A., R. Lagerquist, D. Gagne, et al. 2019. "Making the Black Box More Transparent: Understanding the Physical Implications of Machine Learning." *Bulletin of the American Meteorological Society* 100: 2175–2199. https://doi.org/10.1175/BAMS-D-18-0195.1.

Molina, M., T. A. O'Brien, G. Anderson, et al. 2023. "A Review of Recent and Emerging Machine Learning Applications for Climate Variability and Weather Phenomena." *Artificial Intelligence for the Earth Systems* 2, no. 4: e220086. https://doi.org/10.1175/AIES-D-22-0086.1.

NASA/METI/AIST/Japan Spacesystems and U.S./Japan ASTER Science Team. 2019. *ASTER Global Digital Elevation Model V003 [Dataset]*. NASA EOSDIS Land Processes Distributed Active Archive Center. https://doi.org/10.5067/ASTER/ASTGTM.003.

National Science and Technology Center for Disaster Reduction of Taiwan. 2019. 20180823 Heavy Rainfall Disaster Report. Taipei, Taiwan.

Oyama, N., N. N. Ishizaki, S. Koide, and H. Yoshida. 2023. "Deep Generative Model Super-Resolves Spatially Correlated Multiregional Climate Data." *Scientific Reports* 13: 5992. https://doi.org/10.1038/s41598-023-32947-0.

Price, I., and S. Rasp. 2022. "Increasing the Accuracy and Resolution of Precipitation Forecasts Using Deep Generative Models." *arXiv Preprint*. arXiv:2203.12297. https://arxiv.org/abs/2203.12297.

Rampal, N., P. B. Gibson, S. Sherwood, G. Abramowitz, and S. Hobeichi. 2025. "A Reliable Generative Adversarial Network Approach for Climate Downscaling and Weather Generation." *Journal of Advances in Modeling Earth Systems* 17: e2024MS004668. https://doi.org/10.1029/2024MS004668.

Rampal, N., S. Hobeichi, P. B. Gibson, et al. 2024. "Enhancing Regional Climate Downscaling Through Advances in Machine Learning." *Artificial Intelligence for the Earth Systems* 3: 230066. https://doi.org/10.1175/AIES-D-23-0066.1.

Reichstein, M., G. Camps-Valls, B. Stevens, et al. 2019. "Deep Learning and Process Understanding for Data-Driven Earth System Science." *Nature* 566: 195–204. https://doi.org/10.1038/s41586-019-0912-1.

Rivoire, P., O. Martius, and P. Naveau. 2021. "A Comparison of Moderate and Extreme ERA-5 Daily Precipitation With Two Observational Data Sets." *Earth and Space Science* 8: e2020EA001633. https://doi.org/10.1029/2020EA001633.

Roberts, N. M., and H. W. Lean. 2008. "Scale-Selective Verification of Rainfall Accumulations From High-Resolution Forecasts of Convective Events." *Monthly Weather Review* 136: 78–97. https://doi.org/10.1175/2007MWR2123.1.

Rocha Rodrigues, E., I. Oliveira, R. Cunha, and M. Netto. 2018. "DeepDownscale: A Deep Learning Strategy for High-Resolution Weather Forecast." In *2018 IEEE 14th International Conference on e-Science (e-Science)*, 415–422. IEEE. https://doi.org/10.1109/eScience.2018.00130.

Ronneberger, O., P. Fischer, and T. Brox. 2015. "U-Net: Convolutional Networks for Biomedical Image Segmentation." In *Medical Image Computing and Computer-Assisted Intervention – MICCAI 2015. MICCAI 2015. Lecture Notes in Computer Science*, edited by N. Navab, J. Hornegger, W. Wells, and A. Frangi, vol. 9351. Springer. https://doi.org/10.1007/978-3-319-24574-4_28.

Saha, A., and S. Ravela. 2022. "Downscaling Extreme Rainfall Using Physical-Statistical Generative Adversarial Learning." *arXiv*. https://doi.org/10.48550/arXiv.2212.01446.

Sha, Y., D. J. Gagne II, G. West, and R. Stull. 2020. "Deep-Learning-Based Gridded Downscaling of Surface Meteorological Variables in Complex Terrain. Part II: Daily Precipitation." *Journal of Applied Meteorology and Climatology* 59: 2075–2092. https://doi.org/10.1175/JAMC-D-20-0058.1.

Shi, W., J. Caballero, F. Huszar, et al. 2016. "Real-Time Single Image and Video Super-Resolution Using an Efficient Sub-Pixel Convolutional Neural Network." In *2016 IEEE Conference on Computer Vision and Pattern Recognition (CVPR)*, 1874–1883. IEEE. https://doi.org/10.1109/CVPR.2016.207.

Sillmann, J., V. V. Kharin, X. Zhang, F. W. Zwiers, and D. Bronaugh. 2013. "Climate Extremes Indices in the CMIP5 Multimodel Ensemble: Part 1. Model Evaluation in the Present Climate." *Journal of Geophysical Research: Atmospheres* 118: 1716–1733. https://doi.org/10.1002/jgrd.50203.

Soares, P. M. M., D. Maraun, S. Brands, et al. 2019. "Process-Based Evaluation of the VALUE Perfect Predictor Experiment of Statistical Downscaling Methods." *International Journal of Climatology* 39: 3868–3893. https://doi.org/10.1002/joc.5911.

Sun, A. Y., and G. Tang. 2020. "Downscaling Satellite and Reanalysis Precipitation Products Using Attention-Based Deep Convolutional Neural Nets." *Frontiers in Water* 2: e536743. https://doi.org/10.3389/frwa.2020.536743.

10970088, 2026, 0, Downloaded from https://rmets.onlinelibrary.wiley.com/doi/10.1002/joc.70607. By Statens Beredning, Wiley Online Library on [20/10/2026]. See the Terms and Conditions (https://onlinelibrary.wiley.com/terms-and-conditions) on Wiley Online Library for rules of use; OA articles are governed by the applicable Creative Commons License

Sun, L., and Y. Lan. 2021. "Statistical Downscaling of Daily Temperature and Precipitation Over China Using Deep Learning Neural Models: Localization and Comparison With Other Methods." *International Journal of Climatology* 41: 1128–1147. https://doi.org/10.1002/joc.6769.

Themeßl, M. J., A. Gobiet, and G. Heinrich. 2012. "Empirical-Statistical Downscaling and Error Correction of Regional Climate Models and Its Impact on the Climate Change Signal." *Climatic Change* 112: 449–468. https://doi.org/10.1007/s10584-011-0224-4.

Thrasher, B., E. P. Maurer, C. McKellar, and P. B. Duffy. 2012. "Technical Note: Bias Correcting Climate Model Simulated Daily Temperature Extremes With Quantile Mapping." *Hydrology and Earth System Sciences* 16: 3309–3314. https://doi.org/10.5194/hess-16-3309-2012.

Tiwari, H., and R. D. Garg. 2025. "Improving Satellite and Reanalysis Precipitation Estimates in a Himalayan River Basin: A Comparative Study of Bias Correction Methods With Focus on Extremes and Ensemble Method Performance." *Environmental Earth Sciences* 84: 632. https://doi.org/10.1007/s12665-025-12626-1.

Tung, Y.-S., C.-Y. Wang, S.-P. Weng, and C.-D. Yang. 2022. "Extreme Index Trends of Daily Gridded Rainfall Dataset (1960-2017) in Taiwan." *Terrestrial, Atmospheric and Oceanic Sciences* 33: 8. https://doi.org/10.1007/s44195-022-00009-z.

Vandal, T., E. Kodra, and A. R. Ganguly. 2019. "Intercomparison of Machine Learning Methods for Statistical Downscaling: The Case of Daily and Extreme Precipitation." *Theoretical and Applied Climatology* 137: 557–570. https://doi.org/10.1007/s00704-018-2613-3.

Vandal, T., E. Kodra, S. Ganguly, A. Michaelis, R. Nemani, and A. R. Ganguly. 2017. "DeepSD: Generating High Resolution Climate Change Projections Through Single Image Super-Resolution." In *Proceedings of the 23rd ACM SIGKDD International Conference on Knowledge Discovery and Data Mining*, 1663–1672. Association for Computing Machinery. https://doi.org/10.1145/3097983.3098004.

Vaswani, A., N. Shazeer, N. Parmar, et al. 2017. "Attention is All You Need." *arXiv Preprint*. arXiv:1706.03762. https://arxiv.org/abs/1706.03762.

Vogel, E., F. Johnson, L. Marshall, et al. 2023. "An Evaluation Framework for Downscaling and Bias Correction in Climate Change Impact Studies." *Journal of Hydrology* 622: 129693. https://doi.org/10.1016/j.jhydrol.2023.129693.

Wang, F., D. Tian, and M. Carroll. 2023. "Customized Deep Learning for Precipitation Bias Correction and Downscaling." *Geoscientific Model Development* 16: 535–556. https://doi.org/10.5194/gmd-16-535-2023.

Wang, F., D. Tian, L. Lowe, L. Kalin, and J. Lehrter. 2021. "Deep Learning for Daily Precipitation and Temperature Downscaling." *Water Resources Research* 57: e2020WR029308. https://doi.org/10.1029/2020WR029308.

Weng, S.-P., and C.-D. Yang. 2018. "The Construction and Verification of Daily Gridded Rainfall Dataset (1960-2015) in Taiwan." *Taiwan Water Conservation* 66: 33–52 (in Chinese With English abstract).

Wernli, H., M. Paulat, M. Hagen, and C. Frei. 2008. "SAL—A Novel Quality Measure for the Verification of Quantitative Precipitation Forecasts." *Monthly Weather Review* 136: 4470–4487. https://doi.org/10.1175/2008MWR2415.1.

Westra, S., H. J. Fowler, J. P. Evans, et al. 2014. "Future Changes to the Intensity and Frequency of Short-Duration Extreme Rainfall." *Reviews of Geophysics* 52: 522–555. https://doi.org/10.1002/2014RG000464.

Wood, A. W., E. P. Maurer, A. Kumar, and D. P. Lettenmaier. 2002. "Long-Range Experimental Hydrologic Forecasting for the Eastern United States." *Journal of Geophysical Research: Atmospheres* 107, no. D20: 4429. https://doi.org/10.1029/2001JD000659.

Zhang, X., L. Alexander, G. C. Hegerl, et al. 2011. "Indices for Monitoring Changes in Extremes Based on Daily Temperature and Precipitation Data." *WIREs Climate Change* 2: 851–870. https://doi.org/10.1002/wcc.147.

Supporting Information

Additional supporting information can be found online in the Supporting Information section. **Table S1:** Seasonal performance of the standard U-Net baseline, corresponding to Tables 3 and 4. The table summarizes the spatial correlation coefficient (CORR) and root mean square error (RMSE; values in parentheses) for seasonal mean rainfall and the three ETCCDI precipitation indices (RX10mm, CDD, and RX1day) over the validation and test periods. The U-Net model was trained and evaluated using the same datasets and experimental setup as the proposed EDA framework, providing a direct comparison with the results presented in the main text. Boldface values indicate that the U-Net achieves the best performance among all three methods (U-Net, EDA, and BCSD) for the corresponding metric, season, and evaluation period. **Figure S1:** Seasonal distributions of the annual maximum 1-day precipitation (RX1day) produced by the standard U-Net baseline over Taiwan during the test period. (a) Seasonal climatological RX1day. (b) Difference between the U-Net and TCCIP observations (U-Net − Obs). The spatial correlation coefficient (CORR) and root mean square error (RMSE; mm/day) are indicated in the lower-right corner of each panel. **Figure S2:** Daily rainfall distributions produced by the U-Net benchmark for four representative extreme-rainfall days during the test period. From left to right, the panels show May 22, 2020, August 24, 2018, August 23, 2018, and August 24, 2019. Rainfall is shown in mm day-1, using the same geographical domain and daily-rainfall colour scale as the corresponding manuscript figure. **Figure S3:** Seasonal Fractions Skill Score (FSS) of daily rainfall for the four downscaling methods (BCSD, EDA, EDA_PR, and U-Net) relative to TCCIP at neighbourhood scales of 5–45 km. Results are shown separately for the five Taiwan rainfall seasons: spring (15 February–15 May), first wet season (16 May–24 July), second wet season (25 July–27 September), autumn (28 September–1 December), and winter (2 December–14 February). Three figures are presented using rainfall thresholds of (a) ≥ 1 mm/day and (b) ≥ 50 mm/day. FSS ranges from 0 to 1, with larger values indicating better spatial agreement between the simulated and observed rainfall occurrence. **Figure S4:** Attention map visualization for the May 22, 2020 Meiyu extreme rainfall event. The top row presents the input ERA5 rainfall (tp) and 10-m wind components (u10 and v10). The remaining panels show the attention weights from six attention heads across four encoder layers for a representative output grid point (cross). The colour scale denotes normalized attention relative to a uniform distribution.

10970088, 2026, 0, Downloaded from https://rmets.onlinelibrary.wiley.com/doi/10.1002/joc.70607. By Statens Beredning, Wiley Online Library on [20/10/2026]. See the Terms and Conditions (https://onlinelibrary.wiley.com/terms-and-conditions) on Wiley Online Library for rules of use; OA articles are governed by the applicable Creative Commons License